The Magnetism of Charge-Stripe Ordered Nickelates

Jack Lee Hanson

A thesis submitted in partial fulfilment
of the requirements for the degree of
Master of Science (by Research)

Jeremiah Horrocks Institute for Maths, Physics and Astronomy
University of Central Lancashire

December 2019

Declaration

Type of Award: Master of Science (by Research)

School: Physical Sciences and Computing

I declare that while registered as a candidate for the research degree, I have not been a registered candidate or enrolled student for another award of the University or other academic or professional institution.

I declare that no material contained in the thesis has been used in any other submission for an academic award and is solely my own work.

No proof-reading service was used in the compilation of this thesis.

Jack Lee Hanson

December 2019

Abstract

The work presented in this thesis uses neutron scattering and magnetization techniques to investigate the magnetic ordering processes and magnetic excitations of charge-stripe ordered $La_{2-x}Sr_xNiO_{4+\delta}$.

When investigating the magnetic ordering, a $x = 0.37$ sample has been studied using neutron diffraction and magnetization measurements. The results from these investigations have been compared to earlier work on a samples with doping levels of $x = \frac{1}{3}$, where commensurate charge-stripe order is the most stable, and $x = 0.275$, which is incommensurately charge-stripe ordered. In studying the temperature evolution of the magnetic Bragg peak widths of both of these samples, an anomalous broadening was observed on cooling. This broadening indicates that there is a reduction of magnetic correlation length. The magnetic order is anticipated to stabilise at these lower temperatures, where the thermal energy is removed from the system, reducing the amount of lattice vibrations that perturb the magnetic order. From neutron diffraction and magnetization measurements a new possible transition has been identified, this transition is linked to the changing periodicity of the charge order.

The correlation lengths and percentage broadening of the magnetic Bragg peak widths in both the $x = 0.275$ and $x = 0.37$ samples, has also been compared both in-Ni-O-plane and out-of-Ni-O-plane on cooling. In doing so, a thermal hysteresis effect was observed in the $x = 0.37$ sample, leading to further disorder of the magnetic

order. Whilst the in-Ni-O-plane broadening suggests a clear reduction of in-Ni-O-plane magnetic correlation length, clearly observed in the $x = 0.37$ sample. The similarities and differences in the magnetic ordering processes of both samples will be discussed throughout this thesis.

Inelastic neutron scattering was used to study the magnetic excitations of charge-stripe ordered $La_{2-x}Sr_xNiO_{4+\delta}$, to see if the magnetic excitations respond to the changing periodicity of the charge-stripe order as we would expect theoretically. In doing so, it has been observed that only magnetic excitations induced at the lowest energy transfers appear to kink to track the changing periodicity. However, magnetic excitations with transfers of energy 3 meV or greater, appear unaffected by this changing magnetic order and as so, no longer kink.

From this work, it is clear that to fully understand the charge-stripe order in $La_{2-x}Sr_xNiO_{4+\delta}$ a range of doping levels must be studied. These being $< \frac{1}{3}$, $= \frac{1}{3}$ and $> \frac{1}{3}$.

Contents

Acknowledgements

I would like to thank a great number of people at this time, whether it be for their help, wisdom or support. Most notably, my Director of Studies, Dr. Paul Freeman and Second Supervisor, Dr. Tim Mercer for their time, knowledge and faith. I would also like to thank the Instrument Responsible at my time at the I.L.L, Stéphane Raymond for his help with the instrumentation of the main experiment highlighted in this thesis.

I would also like to thank the Doctoral and other Masters candidates I shared an office with and made my studies at the University of Central Lancashire enjoyable, these being Simon Smalley, Zoë Henderson, Conor Moorfield, Jordan Cole, Callum Mackinnon and Karl Serjeant.

It goes without saying that the achievements I have or will go on to make would not have been possible without the unwavering love and support of my family, proving that truly anything is possible if you try hard enough, want it badly enough and are prepared to let absolutely nothing stop you from achieving these goals.

Special thanks go to my Mum, Jamie, Liv, Mil & Elsie... this one's for you guys.

Chapter 1

Introduction

1.1 High Temperature Superconductivity and Charge-Stripe Order

Superconductivity has long been a subject of intrigue. The feature of superconductors that draws interest to the field is the fact that a superconductive materials resistance falls to zero[1] below its critical temperature, T_c,[2] and therefore, electrical current is able to flow through it without loss of electrical power. It is for this reason that superconductors have many potential applications in laboratories, industry and in the household such as electrical wiring and M.R.I machines. This can only be fully realised if superconductors with both a high T_c and a high critical current, I_c, are discovered.

Until as recently as *Bednorz* and *Müeller* discovery in 1986, the field of superconductivity was thought to be all but understood.[3] Their discovery of a 'high temperature' superconductor, $La_{2-x}Ba_xCuO_4$, that was observed to operate as a superconductor up to temperatures of 30 K,[4] attracted a significant amount of interest in the field. As this material is based off layers of CuO in a square lattice, it, along

with other CuO based superconductors became known as cuprates. Unlike conventional superconductors, cuprates contain a magnetic ion, the copper, Cu^{2+}. In contrast, conventional superconductors follow the accepted Bardeen-Cooper-Schrieffer Theory, (B.C.S), that predicts a material cannot display both magnetic and superconductive components.[3] In the cuprates, upon entering the superconducting state, a magnetic excitation that was observed to be resonantly sharp in energy can be seen to occur at specific energy and wave vector and is now known as the resonance. This observation strongly suggests that the magnetism of the cuprate materials is a root cause of their superconductivity.[5]

High temperature superconductors have many potential applications.[1] However, in the case of cuprates, they are brittle ceramics and so cannot be easily shaped into wires and tapes for use. Cuprates are also antiferromagnetic, (AFM), and undoped cuprates can be classified as Mott insulators. Some cuprates, when doped with either electrons or holes, can become superconducting.

Electron holes come about through means of chemical substitution, doping, which changes the materials electronic concentration, in the case of the materials studied in this thesis, by replacing a La atom with an Sr atom, introducing one hole into the material. Excess Oxygen can also contribute to the amount of hole doping, two holes are provided per Oxygen site. These holes are the absence of electrons in the valence band of the material and as so can be treated as positive charges, relative to the electrons they share the electronic bands with. For this reason, these holes are able to interact with one another via the Coulomb interaction. The repulsion that occurs between these similarly charged holes cause lines of approximately equidistant charge to form, known as charge-stripes, which in turn minimize the interaction perpendicular to the charge-stripe direction within the Ni-O-plane.[6] In the case of the nickelate used, these electron holes reside predominantly on the Nickel sites of the Ni-O plane.[6] However, in some cases, these holes can be found to form on the

Oxygen sites.[7] Upon cooling, the Nickel atoms between the charge-stripes are observed to magnetically order in a antiferromagnetic array, and the charge-stripes act as anti-phase domain walls for the magnetic order.[8]

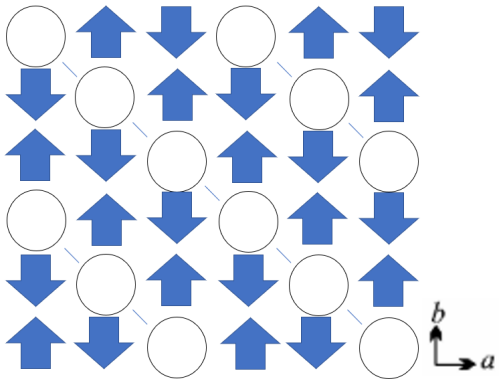

Figure 1.1: Shows both magnetic and charge-stripe order in the 2D Ni-O plane of LSNO.[9] The circles in the figure represent holes on Ni^{3+} sites, whilst the arrows represent Ni^{2+} spins.

Two decades ago, *Tranquada et al.* discovered Charge-Stripe Order, (C.S.O), in a non-superconducting cuprate, $La_{1.48}Nd_{0.4}Sr_{0.12}CuO_4$.[10] It is believed that charge-stripes are intertwined with the superconductive properties of cuprate materials.[11] In the cuprates, the magnetic excitations observe fluctuations similar to spin stripes in cuprates without spin stripe order, making it difficult to understand the magnetic excitations, as we do not have the structure required to observe these excitations.[11] It is for this reason that the charge-stripe ordered nickelate material, $La_{2-x}Sr_xNiO_4$, (LSNO), which has static, long-range, spin stripe order[8] with no superconducting component to complicate the study of C.S.O, will be investigated in this thesis.

The properties of the charge-stripes differ in both the nickelates and the cuprates. In the nickelates, the charge-stripes are observed to be stable due to higher charge-stripe and spin-stripe ordering temperatures, long correlation lengths[8] as well as being aligned along diagonals in the square lattice of the Ni-O plane. Contrary to this, in the superconducting cuprates, the charge-stripes are found to be dynamic and are aligned both horizontally as well as vertically in the square lattice of the

Cu-O plane[11,12] above the lower critical concentration, $x_c \approx 0.055$.[12]

The nickelate sample itself is non-superconductive, as there is one hole per Nickel site, in comparison to one hole per two Copper sites, this half filling means that the cuprates are metallic.[10] Although C.S.O was first observed in the cuprates in 1995,[10] their discovery in the Sr-doped nickelates came two years earlier, in 1993, by *Chen et al.* by means of electron diffraction and was observed for both $x = \frac{1}{2}$ and $x = \frac{1}{3}$ in $La_{2-x}Sr_xNiO_{4+y}$.[13]

1.2 Motivation Behind Thesis

Interest in C.S.O comes from the discovery of a charge-stripe ordered phase in a layered cuprate that was non-superconducting.[10,14] The work in this thesis has been done to better understand C.S.O in the insulating nickelates, to gain a further understanding of C.S.O in cuprate materials, which display high-temperature superconductivity. It is thought that this spin stripe ordered phase alongside the instabilities which originate from the pairing of stripe electrons could lead to the superconductivity observed in the cuprates,[15,16] it is for these reasons that C.S.O needs to be understood.

The same charge-stripes observed in the pseudo-isostructural,[17] La based, '214', cuprates, have also been observed to affect the magnetic structure of LSNO. The charge-stripes acting as an anti-phase domain wall affect the magnetic ordering as after the first charge-stripe changes the direction of the spin adjacent to the stripe, whilst the second stripe changes the direction of the spin back to what we would expect to see in the parent material, La_2NiO_4.

In the cuprates, it has also been observed that the charge-stripe order rotates from being at 45°[4] to the Cu-O bonds when the material is non-superconducting, to parallel to these bonds when superconducting upon increasing the doping level.[11]

This would further suggest that the C.S.O and the superconducting state are somehow linked to one another and so, as we further our knowledge of C.S.O, we also further our understanding of the superconducting mechanism in the cuprates. Furthermore, C.S magnetic fluctuations in La based cuprates also exists over a broad range of doping levels, into the superconducting doping levels.[18] In the cuprates, the superconducting state is suppressed by the long range static spin stripe order.[8] However, in these materials, the magnetic excitations observe fluctuations similar to that of cuprates that do not display spin stripe order. These fluctuations are consistent with a superconducting state.

In LSNO, the C.S.O causes the magnetic Bragg peaks to be centred at: $((\frac{h\pm\varepsilon}{2}),(\frac{k\pm\varepsilon}{2}),l)$, were h,k and l are the Miller indices, parallel to x,y and z of the crystals structure, in real space, which take integer values, and ε is known as the incommensurability. From the incommensurability, the periodicity, P, of the charge-stripes in the LSNO sample can be determined by taking the reciprocal of the incommensurability, $P=\frac{1}{\varepsilon}$.[19]

According to theory, we would expect the ε of the C.S.O, with one hole per Nickel site, where the C.S.O is predominantly centred, should be equal to the doping level, $\varepsilon = n_h$, were the hole concentration is given by $n_h = x + 2\delta$, and δ is the off-stoichiometry content of the Oxygen.[18] ε is found to be approximated by n_h, but is not exactly equal, as it is found to be closer to $\frac{1}{3}$ than $\varepsilon = n_h$, as seen in Figure 1.2. Upon warming, it has been experimentally observed that the ε tends to $\frac{1}{3}$.[20] As seen in Figure 1.1, the charge-stripes are at 45°[4] to the Ni-O bonds of the structure, which can be seen in Figure 1.4.

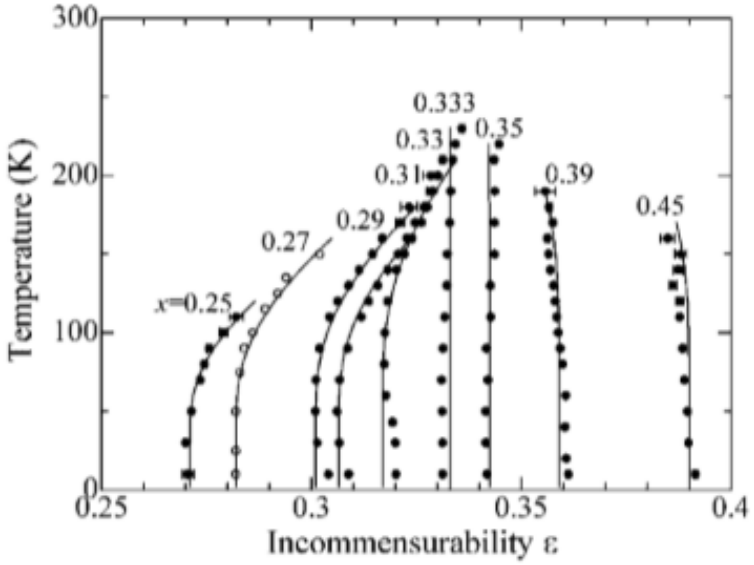

Figure 1.2: The temperature dependence of the incommensurability of the C.S.O in $La_{2-x}Sr_xNiO_4$ at different hole doping levels.[20] The trendlines show a fit to a model which will be examined in Section 3.2.3.

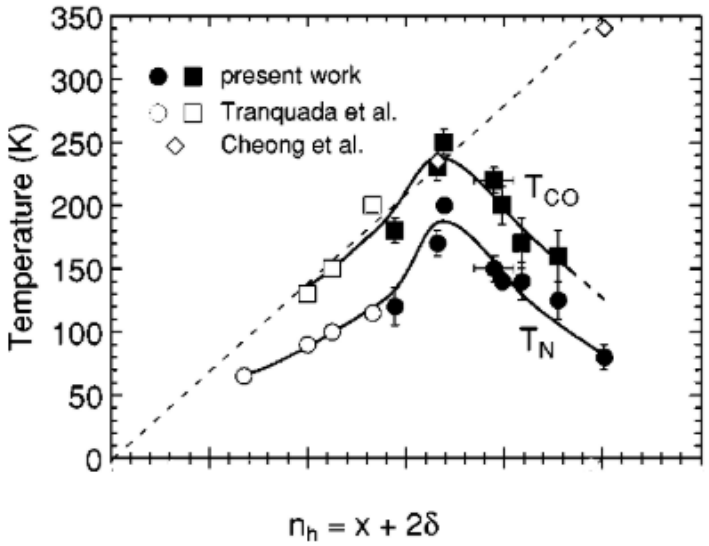

Figure 1.3: The charge ordering temperate, given by squares and diamonds, and the spin ordering temperatures, given by circles, as a function of doping level.[8]

The C.S.O is said to be 'particularly stable' at one third doped,[6,21] as at one

third doping, the C.S.O has the highest charge-stripe and spin-stripe ordering temperatures in LSNO as well as the charge-stripes are commensurately spaced 3-Ni sites apart, thus allowing for a face-centred stacking of the stripes between each of the Ni-O layers due to the out-of-plane Coulomb interaction between parallel charge-stripes of neighbouring Ni-O layers being at a minimum. With slightly 'underdoped' LSNO, $x < \frac{1}{3}$, it can also be seen that the ε tends to one third significantly more than with 'overdoped' LSNO, $x > \frac{1}{3}$.[20] LSNO $x = \frac{1}{3}$, is thought to be stable due to the commensurability effects pinning the charges to the lattice.[22]

In this thesis, the magnetic properties and ordering processes of LSNO will be investigated between temperatures of 2 K and 200 K, the sample will be Sr doped, $x = 0.37$. This will be done by investigating the temperature evolution of the magnetic Bragg peak and magnetic excitations to the known changing periodicity of the charge-stripe structure.[18] These findings will be compared to the unusual temperature dependence of the magnetic order and magnetic excitations in LSNO, with doping levels of both $x < \frac{1}{3}$ and $x = \frac{1}{3}$.[19]

The afore mentioned properties were investigated by making use of the IN12 cold neutron, triple axis spectrometer,[23] (TAS), which is typically used to measure both magnetic excitations as well as the magnetic order. The IN12 is located at the Institut Laue Langevin in Grenoble, France and beam time was in the October of 2018.

1.3 Experimental Details

A single crystal of $La_{1.63}Sr_{0.37}NiO_{4+\delta}$ was used for the experiments, with a mass of $\sim$ 19.4 g. The sample was grown from high purity powders via the floating zone method.[24] Oxygen content of the sample was calculated by means of thermogravimetric analysis and stoichiometric O content has been determined.[25] Diffraction

measurements have revealed that the LSNO adopts a body-centred tetragonal crystal structure for $x > 0.2$,[25] with one La(Sr) site. As there is no evidence in previous diffraction studies of Sr clustering, it is assumed that Sr ions are distributed randomly across the La sites. The crystal has a space group of $I4/mmm$, and has unit cell parameters of a $\approx$ 3.83Å, c $\approx$ 12.72Å.

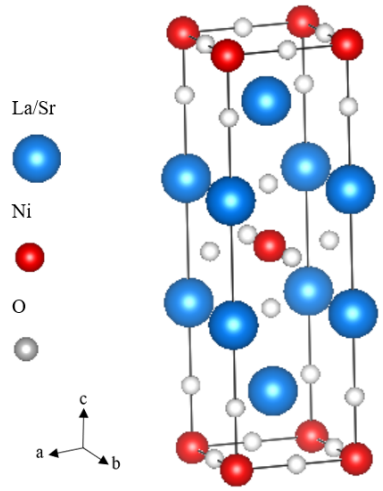

Figure 1.4: The sample material, LSNO, as a B.C.T crystal structure. $a \approx b \approx 3.83$Å, $c \approx 12.72$Å, $\alpha = \beta = \gamma = 90°$.

The cold neutron scattering experiments were performed on the IN12 triple axis spectrometer at the Institut Laue-Langevin. Energies of the neutrons were selected by Bragg reflections from a focused monochromator made of single crystals of Pyrolytic Graphite. A powdered, liquid Nitrogen cooled, Berylium filter was placed between the sample and the analyser such that higher-order harmonics neutrons were minimised. The neutrons were then scattered off the focused analyser, also made of single crystals, such that the energy of the scattered neutrons could be selected. The data were obtained with a final neutron wave vector of 1.5Å^{-1}. The $x = 0.37$ crystal was mounted with [001] and [110] crystal directions in the horizontal scattering plane, such that (h, h, l) positions in reciprocal space could be accessed. Despite the exitation spectrum being essentially two-dimensional, the three components, (h, k, l), of the neutron scattering vector will be listed for the experimental

measurements.

1.4 Instrumentation

For this type of neutron scattering experiment, a TAS is required, the first TAS was designed by Bertram Brockhouse in 1961, for which he was awarded the nobel prize in 1994.[26]

The IN12, located at the Institut Laue-Langevin in Grenoble, France was used as it was able to track the magnetic order through use of elastic neutron scattering as well as the lowest energy magnetic excitations via inelastic neutron scattering. The layout of the IN12 can be seen in Figure 1.5.

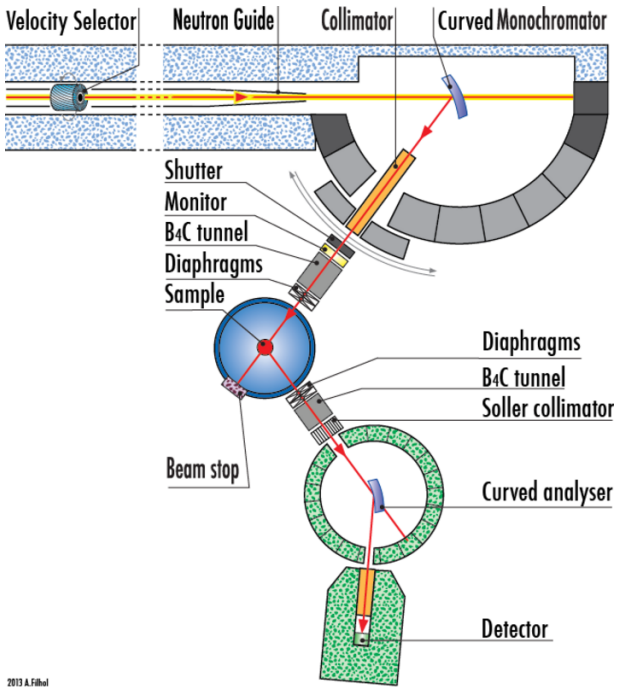

Figure 1.5: The setup of the IN12 cold neutron triple axis spectrometer.[23]

As suggested by the name, the IN12 has three main axes, these being:

- Monochromator Axis
- Sample Axis

- Analyser Axis

All of these axes will now be discussed in detail later in this section, from the neutron source to the detector, to gain a better understanding of the overall experiment.

1.4.1 Neutron Guide

Neutron guides are typically reflective metal alloy, such as Nickel, which has been evaporated on to a glass surface, four of these surfaces are mounted to form a guide tube with a rectangular cross-section. The neutrons passed through the guide, below the neutron guide's critical angle, can be reflected from the neutron guide's surfaces, with a low percentage of neutrons being lost without loss in intensity due to inverse-square laws,[27] this allows the neutrons to travel significant distances from the reactor.

1.4.2 Velocity Selector

The velocity selector, placed inside the neutron guide, ensures a clean beam by preventing higher energy neutrons reaching the monochromator to undergo higher order magnetic Bragg reflections. This is due to the fact that only neutrons with a range of energies and velocities may pass through the guide afterwards.[23,28]

The velocity selector consists of 60 blades, all of which are coated in neutron absorbing ^{10}B, as means of reducing the transmission of false neutrons to $< 10^{-7}$ for wavelengths greater than 2.5Å.[28]

1.4.3 Curved Monochromator

When neutrons arrive at the monochromator, they do so with a variety of energies. Using single crystals of a known crystal, a monochromator can make use of Bragg's

Law.[29]

$$n\lambda = 2d_{hkl}sin\theta$$

To select the appropriate wavelength, λ, neutrons for the incident beam, n is the order of the neutrons, d_{hkl} is the distance between the lattice planes of the selected crystal reflection and θ is the scattering angle of the incident neutrons with respect to the lattice plane. By having neutrons of a given wavelength, the energy of the incident beam of neutrons is defined,[23,30] which will then pass the monitor, which counts the number of incident neutrons that reach the sample and diaphragms and reaching the sample table. The monochromator used by the IN12 was 'double focusing' in order to ensure the highest flux possible was obtained.[28] The term 'double focusing' refers to the directionality of the focusing. The monochromator is curved by moving the crystals so that it is focused, this focusing increases the count rate. The IN12 is simultaneously, vertically and horizontally focused, this curvature approaches ideal Rowland focusing.[26,28]

Vertical focusing of a monochromator considers only the divergence of the neutron beam perpendicular to the scattering plane and has a negligible impact on the energy resolution. However, horizontal focusing with a crystal monochromator simultaneously influences both the imaging properties as well as the wavelength resolution in the scattering plane.[30]

The IN12's monochromator consists of 11 $\times$ 11 crystals of PG(002), with an approximate area of 0.032 m^2 in total.[23] The crystals of PG themselves have a mosaicity of around 0.4° and a thickness of $\sim 2.0 \pm 0.1$ mm. The monochromator is also mounted on rotating and translating tables as well as a goniometer.[28]

1.4.4 Tunnels

Monochromator shielding, of inner diameter 800 mm and composed of 25 cm lead which is further surrounded by a 10 cm borated polyethylene curtain. B_4C elastabore has been added to the inner walls of the lead shielding in an attempt to further absorb neutron radiation from the monochromator.[28] ^{10}B is used as a neutron absorber due to its high cross-section. The tunnels define the neutron flight path, in turn reducing the background radiation from the instrument.

1.4.5 Diaphragms

The diaphragms are made of neutron absorbing B_4C, which blocks out the neutrons, by absorption, that are not going towards the sample position. The diaphragms also defines the scattered beams path to the analyser.

1.4.6 Sample

The LSNO can be placed on a rotating table with tilt goniometers, directly in the path of the beam of incident neutrons, of the selected energy. The sample can then be rotated, such that its lattice planes are orientated with the beam of incident neutrons. These neutrons will then be scattered off the sample.

In order to keep the sample material at the required temperatures, the sample was placed in a standard orange cryostat, capable of both heating or cooling the sample in the 1.5 K - 300 K temperature range.

1.4.7 Curved Analyser

Similar to the monochromator, the analyser axis is made of single crystals of PG(002)[23] and consists of eleven vertical lamellae, driven by a stepper-monitor such that they could be adjusted for horizontal focusing.[31] The analyser is positioned at

the correct scattering angle to select the selected energy of the scattered neutrons. The neutron energy can also be determined by varying the scattering angle away from the analyser. The analyser was placed inside shielding to minimize the neutrons not following the selected flight path reaching the analyser.[26]

To further suppress higher order harmonics, i.e. neutrons of the second and third order, as much as possible, a Berylium filter was used. This was in the form of powder which was cooled by liquid Nitrogen. Be is a low-energy band-pass filter, with an energy cutoff of 5.2 meV, (4 Å), neutrons with energies greater than this are scattered out of the beam.

The analyser was horizontally focusing, The employment of the double focusing monochromator as well as the horizontally focusing analyser has caused an intensity gain of a factor of up to 100, in comparison to flat monochromators and analysers, whilst having a change in energy width of less than a factor of 2.[28]

1.4.8 Detector

The detector employed by the IN12, is two-dimensional and is made up of a single ^{3}He tube and allows for simultaneous scans in Q-ω space to be performed.[31,32]

^{3}He has a high absorption cross section for cold neutrons making it a suitable material for neutron detection. When neutrons are absorbed by ^{3}He, Tritium and a proton are produced as well as the energy of the reaction, which is carried away as kinetic energy of electrons, which are detected as a neutron count in the detector.

Chapter 2

Theory

2.1 Neutron Scattering

Neutrons make an ideal probe for many experiments due to their flexibility. From elastic neutron diffraction experiments, information regarding a materials magnetic order can be obtained. While inelastic neutron scattering can tell us about the magnetic excitations within a material. It is for these reasons that neutron scattering has been the main technique used for the work presented in this thesis.

Unlike neutron scattering techniques, x-ray scattering only probes a material to an order of a few mm as the x-rays strongly interact with the material and so are unable to to obtain any information regarding the magnetic properties of the material. Although x-rays can be used to study the magnetic order and structure of solid crystal samples, as well as magnetic excitations, they lack the energy resolution required to perform this study.

2.2 Properties of a Neutron

Since their discovery in 1932, neutrons have acted as a useful probe for studying magnetism and structure.[1] Other techniques for studying magnetism, such as x-ray

diffraction are more limited in their use and so, magnetic structure is predominantly studied by means of neutron scattering.

Neutrons are uncharged and as such penetrate the bulk of the material,[2] being scattered for the structure off the nuclei by the strong nuclear force. So neutrons readily see both light and heavy atoms. As they emerge from the source, see section 2.2.3, they do so with a variety of energies which is determined by the temperature of the moderator, and as so have the following distribution of Maxwellian velocities:[2]

$$n(\nu) \propto \nu^3 exp\Big(\frac{-\frac{1}{2}m_n\nu^2}{k_BT}\Big)$$

Where ν is the velocity of the neutrons, m_n is the mass of a neutron, k_B is the Boltzmann constant and T is the temperature.

The de Broglie wavelength of a neutron with velocity ν is given by the following equation:[3]

$$\lambda = \frac{h}{m_n\nu'}$$

In the above formula, λ is the de Broglie wavelength, h is the Planck constant, ν' is the velocity of a scattered neutron and as before, m_n is the mass of a neutron. The wavelength is of the same order of magnitude as the interatomic distances for both solids and gasses. Scattering of neutron waves therefore results in interference effects relating to the structure of the scattering system.

As the neutron is a $S = \frac{1}{2}$ particle, it has a non-zero magnetic moment, which means that the neutrons interact with the spins of unpaired electrons of magnetic atoms.[2,3] The elastic scattering from these interactions yields information regarding both the density distribution of the unpaired electrons as well as the how the electronic spins are arranged. Whilst, the inelastic scattering allows us to investigate the time-dependent spin correlations in the system as well as the collective magnetic excitations at different energy transfers.[1]

Cold neutrons also arrive from neutrons passing through a cryogenically cooled moderator, such as solid methane, with a range of energies, 0.1 - 10 meV, and have

a smaller contribution of higher energy neutrons, thus achieving a lower background for instruments.[1] For these reasons, cold neutrons have been used as they can be used to study magnetic excitations at the lowest energy transfers.

2.3 Neutron Sources

In order to investigate the magnetic ordering processes of LSNO $x = 0.37$, a neutron source is required. There are two main types of commonly used neutron source, these being:

- Nuclear Reactor
- Spallation Source

In the case of neutrons produced by a high-flux nuclear reactor, (HFNR), are produced by means of nuclear fission. Nuclear fission is achieved by a neutron being absorbed by a heavy nuclei, ^{235}U in the case of the I.L.L.[4] This will cause the brief formation of ^{236}U, which is unstable and so splits into lighter and more stable nuclei as well as a small number of neutrons and γ rays. The excess neutrons, that are not required to maintain the nuclear fission process can then be used for neutron scattering experiments. The neutron flux in HFNR is assumed to be near isotropic.[1]

The neutrons from a spallation source are produced by high-energy protons, from a synchotron source, striking a heavy metal target, typically Tungsten, W. The sheer impact between the protons and this target causes the nuclei of the metal target to split, which in turn releases a surplus of neutrons suitable for later use in scattering experiments. As the proton beam is pulsed, this means that the neutron beam is also pulsed.[2]

In the case of the work highlighted in this thesis, neutrons from a high-flux nuclear reactor source were selected for use, as in order to focus on the specific

details of the same a continuous beam of neutrons was required. These neutrons will also be used to induce magnetic excitations in the sample at lower temperatures. For this reason, the energy of the incident neutrons will be larger than that of the neutrons that have been scattered. This is known as neutron energy loss scattering, as the neutrons will experience a loss in energy when inducing these excitations.

2.4 Neutron Scattering

To fully understand neutron scattering theory, quantum mechanics must first be applied. In the following section, the main formulae required for neutron scattering will be discussed. A more detailed derivation of these formulae and concepts can be found in the works of *Shirane, Shapiro and Tranquada, 2006,*[1] *Blundell, 2014,*[2] *Squires, 2012*[3] and *Freeman, 2005.*[5]

2.4.1 Neutron Scattering Cross Section

The total neutron scattering cross section, σ, represents the probability that a neutron will be scattered and is given by the formulae:[3,5]

$$\sigma_{tot} = \frac{\text{Number of Neutrons Scattered per Second}}{\Phi}$$

Where Φ is the flux of the incident neutrons. The neutron scattering cross section is the probability of a neutron being scattered. By 'total number', we refer to the number of neutrons scattered in every possible direction.[3]

$$\Phi = \frac{\text{Rate of Neutrons through a Given Area}}{\text{Area}}$$

A typical flux for this sort of experiment is $10^6 - 10^9 n^0 cm^{-2} s^{-1}$. Where, in this case, n^0 is used to denote a neutron and has units of barns, $1b = 10^{-24} cm^{-2}$. However, in the case of the IN12, at the velocity selector, a flux of $8.4 \times 10^7 n^0 cm^{-2} s^{-1}$ is reported.[6]

If we do not wish to study the energies of the scattered neutrons, only count the number of neutrons scattered into the solid angle, $d\Omega$, along the direction θ, ϕ, we would be calculating the differential scattering cross-section.[3] The differential scattering cross-section is the rate of neutrons being scattered into the solid angle $d\Omega$ and is given mathematically by the following formula:

$$\frac{d\sigma}{d\Omega} = \frac{\text{Number of Neutrons Scattered per Second into } d\Omega \text{ in the direction } \theta, \phi}{\Phi \, d\Omega}$$

Measured in bsr^{-1}. It is assumed on many neutron diffraction instruments that the neutrons are losing no energy on being scattered, ie. they are elastically scattered.

In the cases were we do wish to study the direction and energy of the scattered neutrons. It is assumed that the distance between both the counter and target is large in comparison to the dimensions of both the counter and target, such that $d\Omega$, the small angle, is relatively well defined, we would be calculating the partial differential cross-section, making use of the polar coordinates, where the direction of the incident neutrons is the polar axis direction. The partial differential cross-section is proportional to the number of neutrons scattered within a defined energy range and momentum variation into the solid angle,[5] and is given by use of the following formula:[3]

$$\frac{d^2\sigma}{d\Omega dE'} = \frac{\begin{array}{c}\text{Number of Neutrons Scattered per Second into } d\Omega \text{ in the} \\ \text{Direction } \theta, \phi \text{ With a Final Energy Between } E' \text{ and } E' + dE'\end{array}}{\Phi d\Omega dE'}$$

Measured in $bsr^{-1}meV^{-1}$.

2.4.2 Magnetic Elastic Scattering Cross Section

For a Bravais crystal lattice with localised electrons, the coherent, elastic, magnetic scattering differential cross-section, which gives the Bragg peaks, is given by the following formula:[1,3]

$$(\frac{d\sigma}{d\Omega})_{el} = N_M \frac{(2\pi)^3}{\nu_M} \sum_{\mathbf{G_M}} \delta(\mathbf{Q} - \mathbf{G_M}) \left|\mathbf{F}_M(\mathbf{G}_M)\right|^2$$

Where the static magnetic structure factor, $\mathbf{F_M}$, is given by:

$$\mathbf{F_M}(\mathbf{G_M}) = \sum_j p_j S_j e^{i\mathbf{G_M}\cdot d_j} e^{W_j}$$

M has been used as a subscript in order to denote to the magnetic unit cell. N_M and ν_M refer to the number of atoms in the magnetic unit cell and the volume of the unit cell respectively. Here, δ is the Kronecker delta, and $\mathbf{Q}$ and $\mathbf{G}$ refer to the scattering and lattice wave vectors respectively.

2.4.3 Magnetic Inelastic Scattering Cross Section

As inelastic neutron scattering was used to understand the temperature evolution of the magnetic excitations, we must first understand the magnetic inelastic scattering cross section, given by the following formula:[5]

$$(\frac{d\sigma^2}{d\Omega\, dE})_{inel} = (\frac{\gamma r_0}{2})^2 f^2 e^{-2W(\mathbf{Q},T)} \frac{\mathbf{k}}{\mathbf{k'}} S(\mathbf{Q},\omega)$$

Here γ refers to the gyromagnetic ratio, ≈ 1.91, r_0 is the classical electron radius, ≈ 2.8 fm, W is the Debye-Waller Factor and $\mathbf{k}$ and $\mathbf{k'}$ are the intial and final wave vectors of the scattered neutron respectively. When the excitations are localised with a defined energy difference, the scattering function becomes:

$$S(\mathbf{Q},\omega) = \Sigma_{ij}\rho_i \ |\langle j|\hat{u}_\perp|i\rangle|^2 \delta(E_i - E_j - \hbar\omega)$$

Where $|i\rangle, |j\rangle$ are the respective initial and final eigenfunctions of the neutrons with corresponding eigenvalues E_i, E_j of the energy. Here $\hat{u}_\perp$ is the magnetic moment

operator, which is perpendicular to the scattering wave vector, $\mathbf{Q}$ and ρ_i is the thermal population factor of the initial state, which is given by the following:

$$\rho_i = \frac{e^{(\frac{E_i}{k_B T})}}{Z} = \frac{e^{(\frac{E_i}{k_B T})}}{\Sigma_i g_i e^{(\frac{-E_i}{k_B T})}}$$

In this case, the g_i term is the degeneracy of the state, E_i is the energy and Z is the partition function.

In this case, $\frac{\gamma r_0}{2} = 0.2695 \times 10^{-12}$cm, as $r_0 = \frac{e^2}{m_e c^2}$ is the classical electron radius, where e and m_e are the respective charge and masses of an electron, whilst c is the velocity of light.[1,5]

2.5 Magnetic Excitations

At a temperature of 0 K, it is assumed that solids are ordered. However, the atoms that make up this solid are not necessarily static, due to zero-point fluctuations. As the temperature is increased, it is expected that the material will become increasingly more disordered due to lattice vibrations that have been brought about by thermal energy, these vibrations are commonly known as phonons.

If we address the simple case of a ferromagnet, were the magnetic dipole moments are ordered at a temperature of 0 K. At higher temperatures, this ordering is disturbed by the formation of spin waves, otherwise known as magnons. It is possible to produce long-wavelength excitations for very little energy whenever there is broken continuous global symmetry, as the energy cost of the small misalignments between each magnetic moment is small, and these excitations can be deemed 'massless'. Excitations such as these are theoretically understood as Nambu-Goldstone Modes.[2,7]

2.5.1 Magnon Dispersion Relation

Continuing with the case of a isotropic ferromagnet, the magnon dispersion relation can be derived by taking either a semi-classical or a quantum mechanical approach both of which are shown, in depth in *Blundell, 2014*[2] and can be seen in Appendix 1. Both approaches ultimately arrive at the same conclusion:

$$\hbar\omega = 4JS(1 - cos(qa))$$

Which is the dispersion relation for spin waves, where J is the exchange constant, S is the spin quantum number, q is the wave vector and a is the lattice constant of the magnetic order. A physical representation of these spin waves can be seen in Figure 2.1.

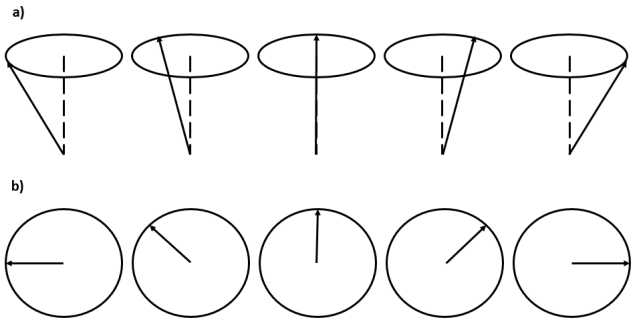

Figure 2.1: (a) A perspective view of a spin wave on a line of spins, (b) a view from above of a spin wave on a line of spins.[2,3]

In the case of a one-dimensional antiferromagnet, the magnon dispersion relation is given by the following expressions, a full derivation is shown in the works of *Kittel, 2005*[8]:

$$\hbar\omega = 4JS|sin(qa)|$$

In the case of the LSNO $x = 0.275$ sample, *Woo et. al, 2005* have determined that $J = 27.5 \pm 0.4$ meV which was obtained from a fit of the data.[9]

2.5.2 Measuring a Spin Wave

While elastic neutron scattering yields information relating to a materials magnetic order and structure, inelastic neutron scattering measures spin wave dispersions.[2] The magnitude of the incident neutron and scattered neutrons neutron wave vector are no longer equal, ie. $\mathbf{k} \neq \mathbf{k'}$. After being scattered, the energy of the neutron can also be found to change from:

$$E = \frac{\hbar^2 k^2}{2m_n}$$

before scattering, to:

$$E' = \frac{\hbar^2 k'^2}{2m_n}$$

after being scattered. This is due to the incident neutron inducing a excitation within the material, of energy, $E = \hbar\omega$, and wave vector, $\mathbf{q}$. Conservation laws regarding both the energy and the momentum are the following:

$$E = E' + \hbar\omega$$

and

$$\mathbf{k} = \mathbf{k'} + \mathbf{q} + \mathbf{G}$$

Here, $\mathbf{G}$ is the reciprocal lattice wave vector to take into account that we are working in periodic reciprocal space, which is a necessary addition due to the dispersion relation of magnons being periodic in the lattice. The measuring of $\mathbf{k}, \mathbf{k'}, E$ and E' make it possible to determine both the angular frequency and the wave vector of excitations.

Magnons can be measured by inelastic neutron scattering due to having energies typically within the range of $10^{-2} - 10^{-3}$eV. Neutrons have similar energies, ranging from meV to eV, and as so can act as an effective probe for a range of energy scales, from quantum tunneling to transitions within the electronic stricture of a material.[2]

Typically, experiments such as this are performed on a TAS, as mentioned in Chapter 1. This is due to the fact that the angles of the three major axes can all be varied, independent of one another. Thus allowing scattered neutrons, with energies corresponding to a range of ω and $\mathbf{q}$ to be measured,[2] as well as to focus on specific scattering wave vectors and energies.

Chapter 3

Results of Magnetic Order

In this chapter, the temperature evolution of the magnetic Bragg peaks will be studied in depth. The magnetization of the sample will also be studied as a function of temperature, such that any potential transitions are identified.

3.1 Example of Data Produced by Elastic Neutron Scattering

The elastic neutron scattering data typically presents itself in the following form when plotted, see Figure 3.1:

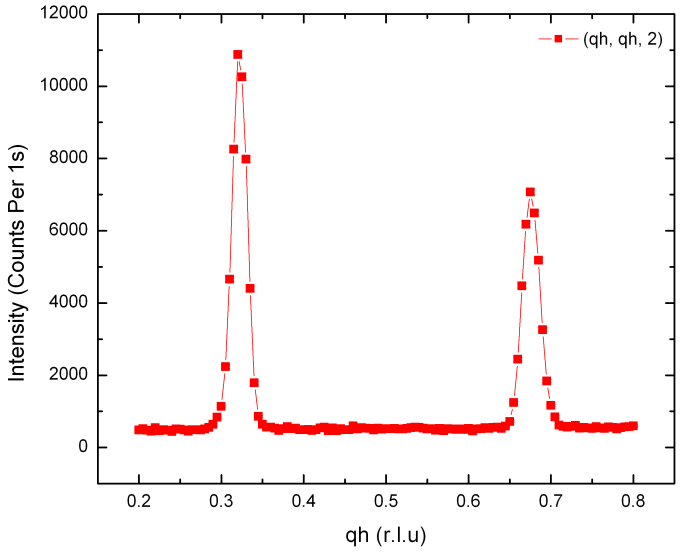

Figure 3.1: A typical plot showing magnetic Bragg peaks produced by elastic neutron scattering along the (h, h, l) scan direction for $l = 2$ at a temperature of 2 K.

Due to the C.S.O, magnetic Bragg peaks can be found to be centred on: $((\frac{h\pm\varepsilon}{2}), (\frac{k\pm\varepsilon}{2}), l)$. As discussed earlier, h, k and l are the Miller indices and are parallel to x, y and z in real space.

3.2 Temperature Evolution

In order to understand the magnetic ordering processes of $x = 0.37$, the temperature evolution of the magnetic Bragg peaks of the $x = 0.37$ sample were studied. Further to this, the temperature evolution of the widths of the magnetic Bragg peaks were specifically investigated to see if any the broadening observed on cooling was linked in any way to the incommensurability of the sample.

3.2.1 Integrated Intensities of the Magnetic Bragg Peaks

The integrated intensities of the peaks studied were calculated by taking the product of the amplitude of the peak and the peaks width, scaled by a monitor count and the resolution corrected peak widths. Neutron diffraction detects the magnetic moments perpendicular to **Q**, the integrated intensity is proportional to the square of the magnetic moments perpendicular to **Q**. We would expect the integrated intensity to decline to close to 0, when approaching T_{SO}, calculated to be 177.5 $\pm$ 2.5 K. However, there is residual intensity above these temperatures. This is likely due to finite energy resolution integrating paramagnons. The low **Q** centre, I will use to refer to the peaks centred near $(0.322, 0.322, l)$, while, I will use high **Q** centre to refer to the peak centred near $(0.676, 0.676, l)$.

Intensity of Low Q Peaks Scanned Parallel to $(h, h, 0)$

If we first study the integrated intensities of the in-Ni-O-plane magnetic Bragg peaks centred near $(0.322, 0.322, l)$, at base temperature, for l values of both 2 and 3 on warming. Starting with the $l = 2$ scan data, we observe the integrated intensity of the peak continuously drops from $\sim$ 800 a.u, at 20 K, to 15 a.u at 180 K. In the temperature range 160 K to 180 K, the gradient at which the intensity drops is reduced.

Now, studying the $l = 3$ data, we observe a similar trend to that of the in-Ni-O-plane, $l = 2$ data. However, the intensities measured at the same temperatures are slightly larger as the $(0.322, 0.322, 3)$ peak is closer to being parallel to $(0, 0, l)$ and probing the full in-plane moment. We observe that the intensity decreases from $\sim$ 1200 a.u at a temperature of 20 K to around 25 a.u at a temperature of 180 K. Again, a slightly shallower gradient can be observed between a temperature range of 160 K and 180 K.

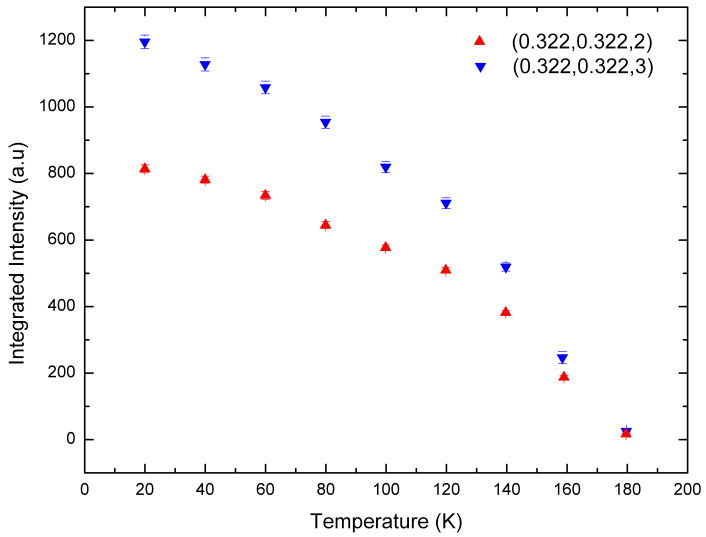

Figure 3.2: The temperature evolution of the integrated intensity of the in-Ni-O-plane peaks centred near $(0.322, 0.322, l)$.

Intensity of High Q Peaks Scanned Parallel to $(h, h, 0)$

If we begin by first studying the temperature evolution on warming of the integrated intensity of the peak centred near $(0.676, 0.676, 0)$ only sensitive to the Ni moment parallel to the charge-stripe direction, as the moments are in Ni-O plane.[1] Between temperatures of 2 K and 20 K, the integrated intensity can be observed to increase from around 425 a.u to 900 a.u, due to a spin reinordering.[1] Following this, the intensity can be seen to continuously decrease until reaching an intensity of $\sim$ 400 a.u at a temperature of 140 K. Beyond this temperature, the integrated intensity reduces at a faster rate, before reaching a near zero minimum at 180 K.

Looking at the $l = 1$ peak, we notice an increase in the integrated intensity between temperatures of 10 K and 20 K, with an approximate increase of 450 a.u. Following this, we see a more typical decline in the integrated intensity upon further warming. This rate of decline is approximately constant until a temperature of 140 K is reached. Beyond 140 K, a moderately sharper decrease in integrated intensity

can be observed, falling from around 600 a.u to virtually nil at 180 K. For $l = 1$, $\mathbf{Q}$ is approximately parallel to $(h, h, 0)$ and as so mostly observes the perpendicular moment, but also observes a small component parallel to the charge-stripes and so, is more intense despite being measured at a larger $|\mathbf{Q}|$.

In the case of the $l = 2$ scan data, we see a similar trend, with one clear exception, between temperatures of 10 K and 20 K, a small drop in the intensity can be observed from $\sim$ 940 a.u to around 815 a.u, the 10 K. Beyond 20 K, the integrated intensity can be observed to steadily decline, as observed with previous l values, until reaching a minimum intensity of approximately 10 a.u at a temperature of 180 K. In the case of $l = 2$, $\mathbf{Q}$ is not particularly close to parallel to $(h, h, 0)$, but it is close enough to observe the spin reorientation.

If we now study the $l = 3$, the sharp drop previously seen between 10 K and 20 K, is no longer observed. However, the rest of the data very clearly displays a similar trend to the previously studied peaks. Dropping from approximately 1000 a.u at temperatures of 10 K and 20 K to a mere 25 a.u at temperatures near 180 K. For $l = 3$, $\mathbf{Q}$ is further away from $(h, h, 0)$ than $l = 2$ and so is probing the parallel moment and a large component of the perpendicular moment and so behaves similarly to $(0.322, 0.322, 2)$.

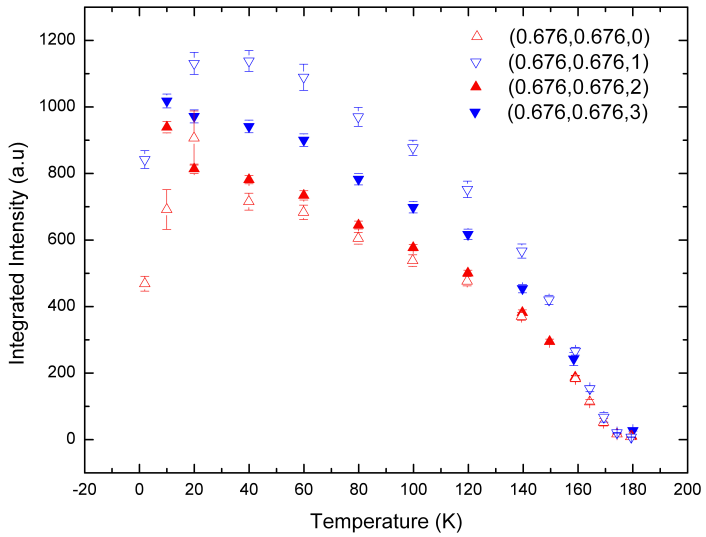

Figure 3.3: The temperature evolution of the integrated intensity of the in-Ni-O-plane peaks centred near $(0.676, 0.676, l)$.

Intensity of Low Q Peaks Scanned Parallel to $(0, 0, l)$

The temperature evolution of the integrated intensity of the magnetic Bragg peak centred near $(0.322, 0.322, 2)$ scanned in the out-of-Ni-O-plane direction will now be investigated. Between temperatures of 2 K and 20 K, an increase in intensity of around 23.1 % can be observed, this is followed by a slight decrease in intensity. Between temperatures of 60 K and 100 K, the integrated intensity can be seen to be approximately constant. This comes before an increase in intensity of approximately 6.9 % between 100 K and 120 K. The intensity can then be observed to suddenly decline to an intensity of $\sim$ 5600 a.u at a temperature of 130 K. The intensity can then be observed to minimally increase at 140 K, before steadily declining to the lowest intensity of 2850 a.u at 160 K. Surprisingly, at 165 K, the integrated intensity can be observed to slightly increase to around 3700 a.u.

Similar to the $(0.322, 0.322, 2)$ magnetic Bragg peak, the integrated intensity of the $(0.322, 0.322, 3)$ Bragg peak can be observed to increase by 30.5 % between

temperatures of 2 K and 20 K, following this, there is a small decline in intensity. Between temperatures of 60 K and 100 K, the intensity increases by around 8.2 %. However, unlike the $(0.322, 0.322, 2)$ magnetic Bragg peak, the intensity steadily declines after reaching a temperature of 100 K, reaching 1250 a.u at a temperature of 165 K.

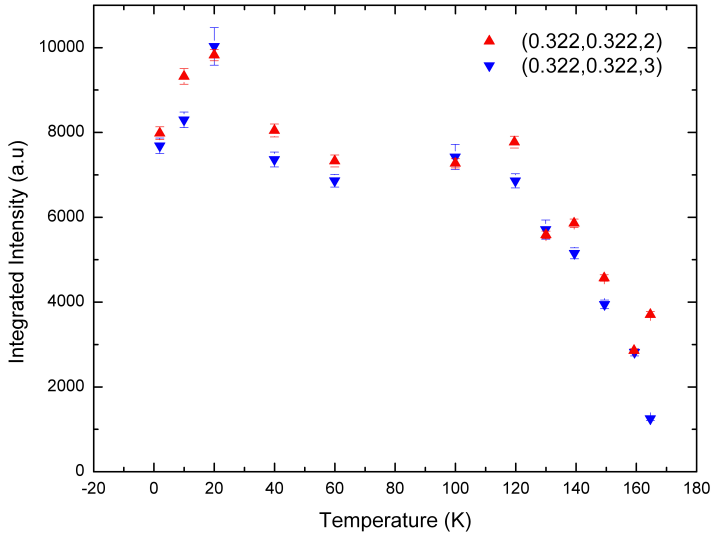

Figure 3.4: The temperature evolution of the integrated intensity of the Out-of-Ni-O-plane peaks centred near $(0.322, 0.322, l)$.

Intensity of High Q Peaks Scanned Parallel to $(0, 0, l)$

If we now study the temperature evolution of the peak centred near $(0.676, 0.676, 0)$ out-of-Ni-O-plane, we observe an increase of close to around 48.5 % between temperatures of 2 K and 20 K. For temperatures exceeding 20 K, we see a very minimal drop in the intensity, before reaching a region of near constant integrated intensity between temperatures of 60 K and 100 K. Following this, we observe a steady decline in the intensity before reaching a minimum intensity of $\sim$ 350 a.u approaching a temperature of 170 K.

The same can be said for the $l = 1$ data, as similar features can be observed in its trend. An increase of 52.3 % in intensity can be observed between temperatures of 2 K and 20 K. Following this, the intensity can be observed to slightly decrease, before again reaching a region, in which there is little change in the overall intensity between 60 K and 100 K. We then observe an all to familiar decline in intensity, were upon reaching a temperature of 170 K, an intensity of approximately 475 a.u is observed.

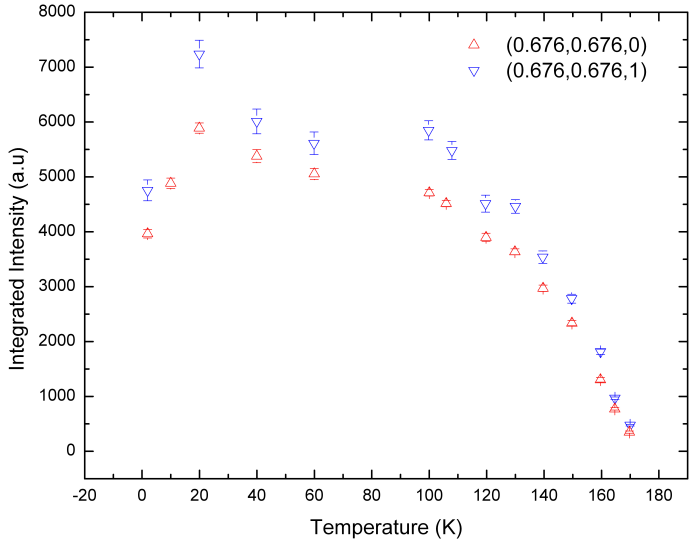

Figure 3.5: The temperature evolution of the integrated intensity of the Out-of-Ni-O-plane peaks centred near $(0.676, 0.676, l)$.

By studying the integrated intensities in the $x = 0.37$ sample, we find that our results are consistent with those previously reported by *Freeman et. al, 2004*.[1]

3.2.2 Positions of the Magnetic Bragg Peak Centres

The in-Ni-O-plane position of the magnetic Bragg peak centre can be used to determine the incommensurability of the LSNO $x = 0.37$ sample material, as seen in Section 3.3. Here, we investigate the temperature evolution of the centre position

of the magnetic Bragg peaks for a variety of l values, $l = 0...3$, for the low and high **Q** centres along the in-Ni-O-plane scan direction.

In-Plane, Low Q Peaks

If we study the peak centred near $(0.322, 0.322, 2)$, we observe a significant increase in the position of the magnetic Bragg Peak centre in the Ni-O-plane. At 20 K, we observed that the peak in centred on approximately 0.322 r.l.u. However, at a temperature of 180 K, we observed that the peak is centred closer to 0.3275 r.l.u. This increase in centre position starts to become particularly obvious at temperatures of 140 K. The same can be said for the peak centred near $(0.322, 0.322, 3)$. The increase in the position of the magnetic Bragg peak centre, whilst slightly smaller, is still rather significant. Starting with a centre position of ~ 0.322 r.l.u at 20 K and reaching a centre position of around 0.3275 r.l.u at 180 K.

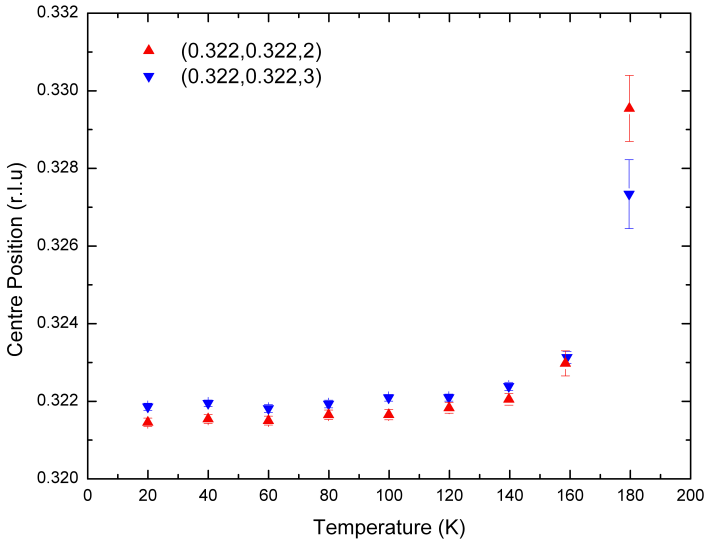

Figure 3.6: The temperature evolution of the in-Ni-O-plane peak centre positions centred near $(0.322, 0.322, l)$.

In-Plane, High Q Peaks

For the magnetic Bragg peak centred near $(0.676, 0.676, 0)$, we observe a gradual decrease in the position of the peak centre between temperatures of 2 K and 60 K. We also observe that the position of the peak centre holds at around 0.6765 r.l.u between temperatures of 60 K and 120 K. However, beyond a temperature of 120 K, the position of the peak centre shifts quite significantly, reaching a minimum of 0.6735 r.l.u, before increasing to a position of 0.675 r.l.u at 165 K.

If we now study the peak observed at the same (h, k) positions, but with $l = 1$ rather than 0, we see that the position of the peak centre is around 0.6765 r.l.u between temperatures of 2 K and 120 K. For temperatures exceeding 120 K, the position of the magnetic Bragg peak centre begins to decline, in a similar fashion to that of the $l = 0$ and $l = 2$ peaks, studied below. However, unlike the $l =$ even peaks, the position of the magnetic Bragg peak does not increase after a temperature of 160 K and reaches a minimum of ~ 0.6725 r.l.u at a temperature of 180 K.

As we would expect, the trend for the $l = 2$ data is very similar to that of the $l = 0$ data. In this case, we observe that the position of the peak centre stays at a similar position between temperatures of 2 K and 100 K, which is followed by a familiar decline to a minimum of 0.6745 r.l.u at 160 K. The position of the magnetic Bragg peak centre can again be seen to increase to around 0.676 r.l.u at 180 K. The same can be said for the $l = 3$ data being similar to that of the $l = 1$ data. However, the position of the peak centre in this case appears unchanged until a temperature of 140 K is exceeded. Beyond 140 K however, a significant decrease in the position of the magnetic Bragg peak centre can be observed, as it can be seen to fall from 0.675 r.l.u at 140 K to 0.6525 r.l.u at 180 K.

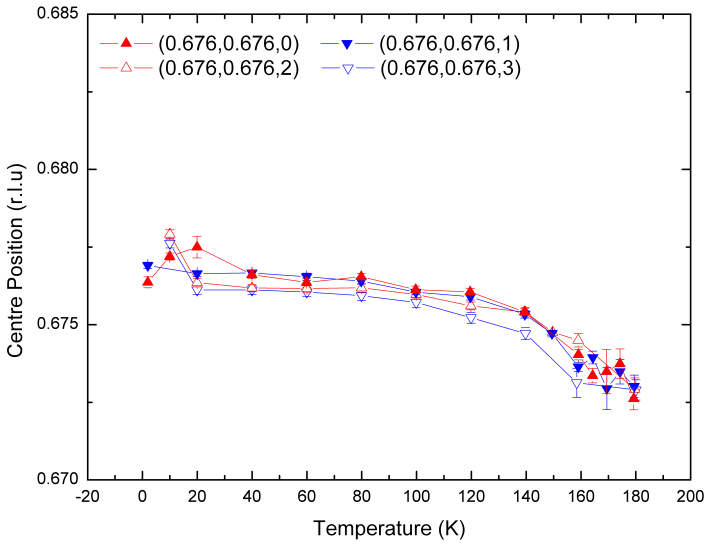

Figure 3.7: The temperature evolution of the in-Ni-O-plane peak centre positions centred near $(0.676, 0.676, l)$.

3.2.3 Incommensurability

The incommensurability, ε, of the sample material is given by the following:

$$\varepsilon \approx n_h + 2\delta$$

Where n_h is the hole doping concentration and δ is the off-stoichiometry of the O of the sample, it is believed in the $x = 0.37$ that $\delta = 0$.[1] The periodicity of the charge-stripes can be found by taking the reciprocal of the incommensurability, like so:

$$P = \frac{1}{\varepsilon}$$

Incommensurability as a Function of Temperature

As mentioned earlier, both the spin- and charge-ordering temperatures can be found to preferentially tend to $\varepsilon = \frac{1}{3}$.[2] In a study performed by *Ishizaka et. al, 2004*,[2] a

better understanding of the temperature evolution of LSNO samples was obtained for a range of doping levels, $0.25 \leq x \leq 0.4$, and can be seen in Figure 1.2.

Ishizaka et. al, 2004 produced a model to explain this temperature dependence based on the existence of an energy gap, however, this model has a few issues. Largely, the fact that *Ishizaka et. al, 2004* assumed the incommensurability, ε, and the hole concentration, n_h, to be equal, . Previously, in 1999, many members of this group acknowledged that the hole concentration, defined as p in their works, was not in fact equal to the incommensurability.[2] However, in the work from 2004, it is accepted that $\varepsilon = p + \delta$.

Models Used

For the doping levels investigated in this thesis, a similar model to that of *Ishizaka et. al, 2004* [2] has been considered, with one small exception, the hole concentration term, p, has been replaced with the incommensurability when it is similar to that at base temperature, ie. $\varepsilon \approx \varepsilon(0)$. This value was determined by taking twice the modulus of 0.5 minus the value of the position of the magnetic Bragg peak centre, as given by the formula below:

$$\varepsilon(0) = 2 \times |0.5 - \text{Position of Magnetic Bragg Peak Centre (r.l.u)}|$$

When the incommensurabilty is calculated in such a way for all the temperatures studied, not just when the incommensurability is similar to that at 2 K, we are left with the following plots from a previous study of the $x = 0.275$ sample and the new results on $x = 0.37$ sample:

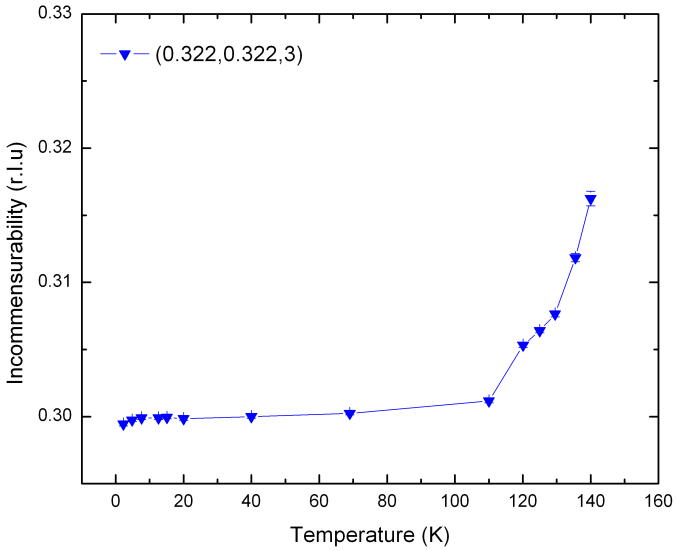

Figure 3.8: The temperature evolution of the incommensurability in $x = 0.275$ using the position of the peak centres.

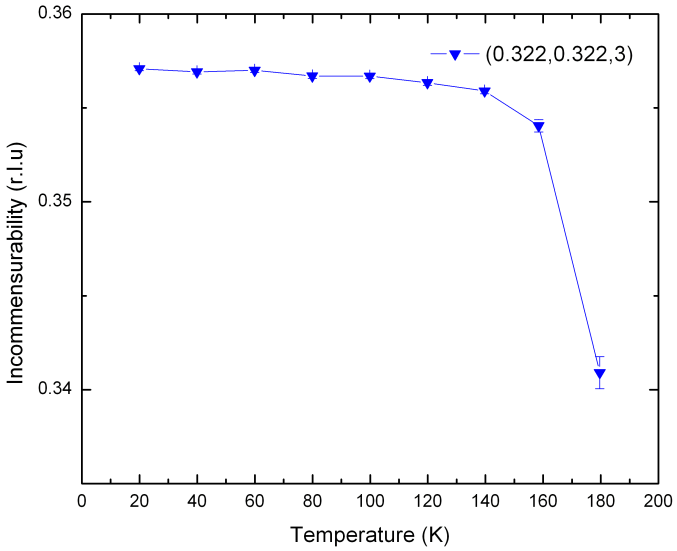

Figure 3.9: The temperature evolution of the incommensurability in $x = 0.37$ using the position of the peak centres.

The temperature evolution of the incommensurability has been calculated for both $x = 0.275$ and $x = 0.37$, using the modified models given below:

$$\varepsilon_{under} = \frac{\varepsilon(0)}{1 - e^{(-E_g/k_BT)}}$$

$$\varepsilon_{over} = \frac{\varepsilon(0) - e^{(-E_g/k_BT)}}{1 - e^{(-E_g/k_BT)}}$$

Here, E_g is the known energy gap in meV, which is doping dependent. In the case of $x = 0.275$, the ε_{under} equation was used to model the temperature evolution of the incommensurability, while the ε_{over} equation was used for the $x = 0.37$ sample. When data is plotted, using these models, the incommensurability can be found to tend to $\frac{1}{3}$, as expected.[2] In doing so, it is made obvious that the incommensurability of an underdoped sample tends to $\frac{1}{3}$ at a far more significant rate than for an overdoped sample.

If we now apply these models to the data collected for both of the doping levels under investigation, we observe slightly different trends:

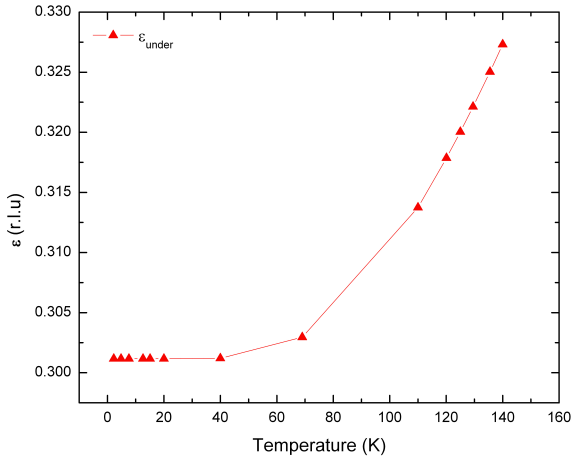

Figure 3.10: The temperature evolution of the incommensurability in LSNO $x = 0.275$ using the adapted *Ishizaka et. al, 2004* models.

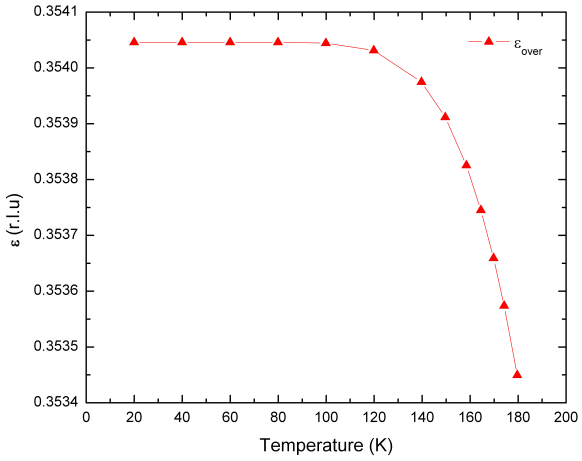

Figure 3.11: The temperature evolution of the incommensurability in LSNO $x = 0.37$ using the adapted *Ishizaka et. al, 2004* models.

3.2.4 Change in Incommensurability as a Function of Temperature

The modulus of the changing incommensurability of both doping levels, $x = 0.275$ and $x = 0.37$, were plotted as a function of temperature such that any differences in the temperature evolution of both samples were apparent. The changing incommensurability was calculated by use of the following:

$$|\Delta\varepsilon| = |\varepsilon(\mathrm{T}) - \varepsilon(0\ \mathrm{K})|$$

When plotted, we are left with the trends seen in Figure 3.12 below:

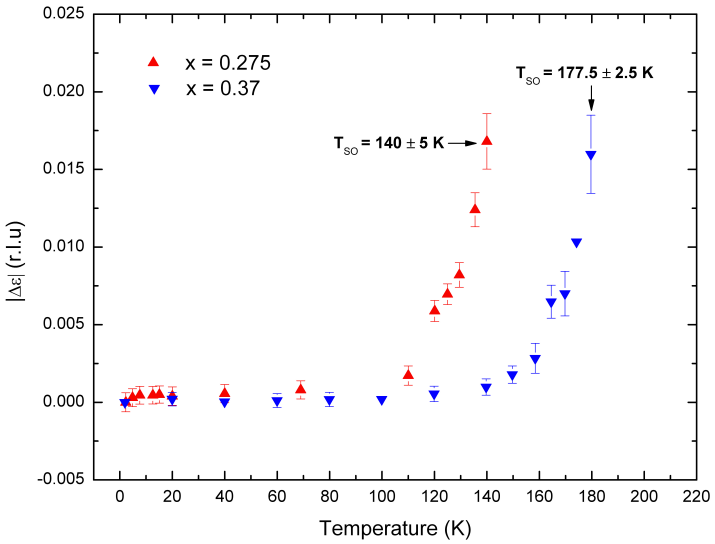

Figure 3.12: The temperature evolution of the changing incommensurability for both $x = 0.275$ and $x = 0.37$ samples.

As expected, when both trends are plotted alongside one another, the spin ordering temperature for the $x = 0.275$ sample is significantly less than that of the $x = 0.37$ sample, with respective spin ordering temperatures of 140 ± 5 K and 177.5 ± 2.5 K.

From Figure 3.12, it is clear that the change in incommensurability of the $x = 0.275$ sample trends upwards somewhat abruptly following its corner temperature, occuring over a temperature range of 10 K - 20 K. However, the incommensurability of the $x = 0.37$ sample trends upwards in a much smoother fashion than that of the $x = 0.275$ sample, for temperatures exceeding the calculated corner temperature, as we see the change occurs over a temperature range of 20 K - 40 K. We define the corner temperature as being the temperature at which the incommensurability of the sample begins to suddenly and very clearly tend to $\frac{1}{3}$.

CHAPTER 3

Determining the Corner Temperature from the Incommensurability Data in LSNO $x = 0.275$

In this thesis, the temperature at which there can be observed to be a sudden 'shoulder' of some variety in the data will be referred to as the corner temperature. The corner temperature was determined by taking two linear temperature regions in the incommensurability data for the $x = 0.275$ sample. The first of the regions used was between 5 K and 70 K and the second, between 130 K and 140 K.

The equations of both of the linear fits were then equated and the corner temperature was calculated by means of simultaneous equation. In doing so, a corner temperature of 112.7 $\pm$ 5.6 K has been calculated for the $x = 0.275$ sample.

Determining the Corner Temperature from the Incommensurability Data in LSNO $x = 0.37$

For the $x = 0.37$ sample, the same logic was applied, as two linear temperature ranges were again plotted and from the equations of these fits, the corner temperature for the sample could be determined. The ranges used in this case were between 20 K and 120 K and between 160 K and 180 K. This was done for both the $(0.322, 0.322, 2)$ and $(0.322, 0.322, 3)$ data sets, both of which yielded minimally different results. For the $l = 2$ data, a corner temperature of 155.0 $\pm$ 4.7 K was calculated. However, for the $l = 3$ data, the corner temperature has been calculated to be 154.1 $\pm$ 4.4 K.

In the case of this work, the corner temperature of 154.11 $\pm$ 0.23 K from the $l = 3$ data will be used to determine the percentage broadening of the peak widths.

3.2.5 Discussion of the Temperature Evolution of Incommensurability

If we fit the *Ishizaka et. al, 2004* models to the data for both the $x = 0.275$ and $x = 0.37$ samples, it is clear that the incommensurability tends to $\frac{1}{3}$ much differently than the model used for determining the corner temperature. The most notable difference being that the *Ishizaka et. al, 2004* models begin to tend to $\frac{1}{3}$ at significantly lower temperatures than our model and do so in a much smoother fashion.

3.2.6 Widths of the Magnetic Bragg Peaks

The temperature evolution of the widths of the magnetic Bragg peaks were studied for both the low and high **Q** magnetic Bragg peaks, for a variety of l values, $l = 0...3$. The reasoning behind this is that the peak widths for $l =$ odd and $l =$ even are anticipated to differ, as we would expect that the $l =$ even peaks be broader than the $l =$ odd peaks.[2] For this reason, all the l values will be studied for both the low and high **Q** magnetic Bragg peaks. All of the peak widths discussed in this study have been corrected for experimental resolution, for more detail see Section 3.2.7.

3.2.7 Resolution Corrections to Peak Widths

In order for the temperature evolution of the peak widths to be truly comparable to other doping levels, the data must first be corrected. These corrections account for the instrumental resolution of the IN12, which was chosen for use due to its flexible scattering geometry allowing the user to determine whether the observations made were valid or instrumental in nature.

These corrections were performed by squaring the observed peak width and subtracting the squared width of the resolution, ie. using the width of the nearest

available structural peak in reciprocal space, the result is to then be square rooted, this is otherwise known as adding widths by quadrature. This method of correction is given by the formula below:

$$\sigma_{int} = \sqrt{\sigma_{obs}^2 - \sigma_{res}^2}$$

The corrected errors on these peak widths could be calculated in a similar fashion, with the exception of rather than subtracting the error of the resolution peak from the error of the observed peak, they should instead be subject to the addition of one another, like so:

$$E_{int} = \sqrt{E_{obs}^2 + E_{res}^2}$$

Each of the parameters are given by the following:

- σ_{int} - Intrinsic Peak Width
- σ_{obs} - Observed Peak Width
- σ_{res} - Resolution Peak Width
- E_{int} - Error in the Intrinsic Peak Width
- E_{obs} - Error in the Observed Peak Width
- E_{res} - Error in the Resolution Peak width

All of the data shown relating to the peak widths has been resolution corrected in this way.

3.2.8 Out-of-Plane Peak Widths

l = odd

If we first study the scan direction parallel to the out-of-plane direction for l = odd. Looking at the magnetic Bragg peak centred near $(0.322, 0.322, 3)$, we observe in

Figure 3.13, that the width of the peak remains somewhat constant between temperatures of 2 K to 100 K, with the exception of the 20 K measurement, with widths of approximately 0.037 r.l.u. At a temperature of 130 K, the peak can be observed to re-sharpen to from a width of 0.045 r.l.u to a width of ~ 0.039 r.l.u. Following this, we observe a broadening, which becomes significant beyond a temperature of 160 K and continues reaching a width of 0.058 r.l.u by 165 K. For both the $(0.676, 0.676, 1)$ and $(0.676, 0.676, 3)$ peaks, we see behaviour consistent with that of the $(0.322, 0.322, 3)$ magnetic Bragg peak. As in the case of all three peaks studied, the same features, such as the region of near constant width between 2 K and 100 K, can be observed.

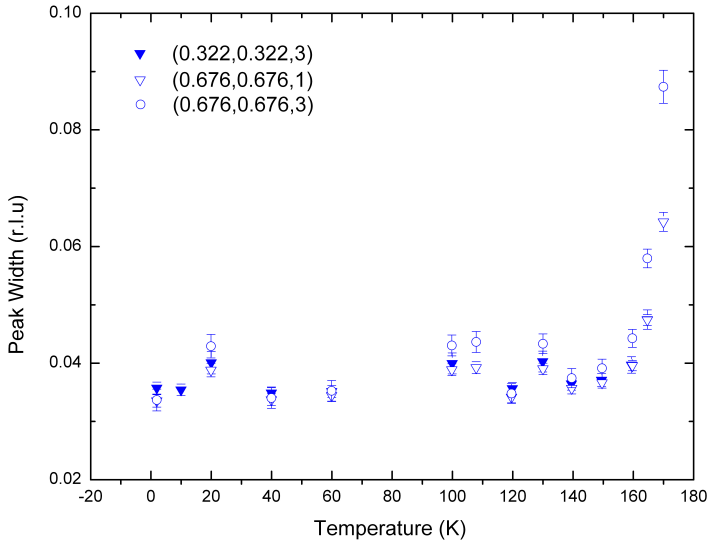

Figure 3.13: The temperature evolution of the Out-of-Ni-O-plane peak widths for l = odd.

l = **even**

If we now study the scan direction parallel to the out-of-plane direction for l = even peaks. We would expect each of the trends to be similar as the case of the l = odd

peaks. For the $(0.322, 0.322, 2)$ magnetic Bragg peak, the peak width can be observed to stay fairly constant, ~ 0.073 r.l.u between temperatures of 2 K and 100 K. However, for temperatures exceeding 120 K, a small sharpening can be observed and continues until a temperature of ~ 150 K is reached. For temperatures exceeding 150 K, the peak can be observed to re-broaden to a width of ~ 0.08 r.l.u by 165 K. Both the $(0.676, 0.676, 0)$ and $(0.676, 0.676, 2)$ magnetic Bragg peaks behave in roughly the same manor as the $(0.322, 0.322, 2)$ peak, showing the peak width is approximately constant between 2 K and 110 K followed by the same sharpening and re-broadening observed between 130 K and 165 K.

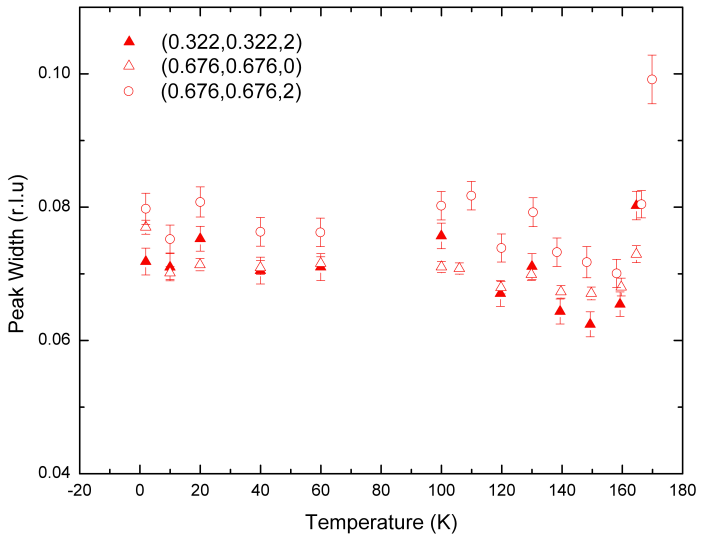

Figure 3.14: The temperature evolution of the Out-of-Ni-O-plane peak widths for l = even.

3.2.9 Discussion of Out-of-Plane Peak Widths

In the case of the out-of-plane peak widths, we observe that the l = even peaks can be observed to broaden on cooling below ~ 140 K, it should be mentioned that for the l = odd peaks out-of-plane, there is very little evidence of any broadening on cooling. Whilst this sharpening is not expected theoretically, it has been observed

previously in LSNO $x = 0.275$[3] and appears to occur below the corner temperature. In this study, a very significant sharpening was observed at close to what is now suspected to the corner temperature of LSNO $x = 0.275$, $\sim$ 110 K.

3.2.10 Reheating Study of Out-of-Ni-O-Plane

As the experiment was conducted, the LSNO $x = 0.37$ sample was measured while warming from base temperature to 180 K. Following this, the sample was cooled back to $\sim$2 K and warmed while measuring, to temperatures of 200 K. This was done in order to improve counting statistics, add more temperatures and in turn, gain further confidence in the results.

It was noticed that the temperature evolution of the out-of-plane peak widths, as seen in Figure 3.14, there was a slight difference between the trends on first warming and reheating. For this reason, it was decided that the data set should be split into these separate sets, such that any differences in the temperature evolution of the out-of-Plane peak widths could be clearly observed.

When studying the out-of-plane peak widths, l values of 2 and 3 were used for the low **Q** peak, while 0, 1, 2 and 3 were used for the high **Q** peak. 0 and 1 were studied in the case of the high **Q** peak to further confirm any observations made in both the l = odd and l = even trends.

Warming, l = odd

When studying the warming data, out-of-Ni-O-plane, we first study the width of the $(0.322, 0.322, 3)$ magnetic Bragg peak. We observe that between temperatures of 2 K and 120 K, the width of the peak barely changes and stays around 0.036 r.l.u. Following this, the peak very briefly broadens at a temperature of 130 K to 0.0455 r.l.u, the peak then sharpens back to its close to its original width before drastically broadening to a maximum of $\sim$ 0.058 r.l.u at a temperature of 165 K. In the case of

both the $(0.676, 0.676, 1)$ and the $(0.676, 0.676, 3)$ magnetic Bragg peaks, we observe behaviour consistent with that of the $(0.322, 0.322, 3)$ peak, as in the case of all three peaks, the widths can be observed to stay approximately constant between 2 K and 120 K, before a clear broadening at $\sim$ 150 K.

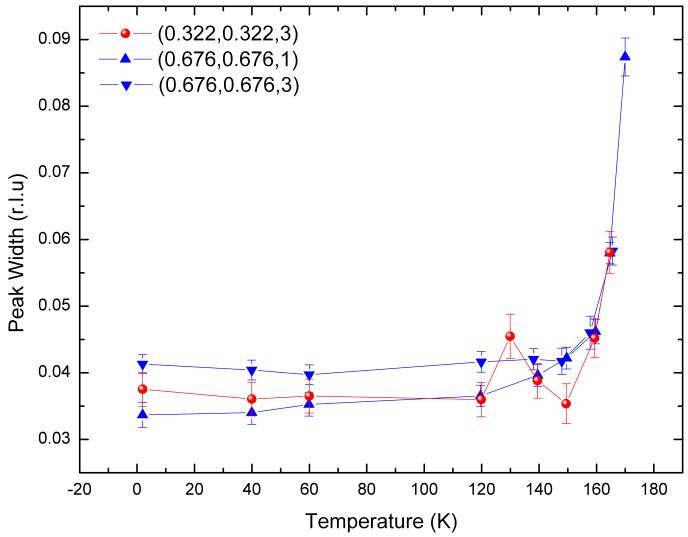

Figure 3.15: The temperature evolution of the Out-of-Ni-O-plane peak widths on first warming for l = odd.

Warming, l = even

If we now study the warming data, out-of-plane for the $(0.322, 0.322, 2)$ magnetic Bragg peak, we observe very little change in the width of the peak in between temperatures of 2 K and 140 K, as the width of the peak stays around 0.069 r.l.u. Exceeding 140 K, there is a sudden sharpening of the peak to a width of 0.062 r.l.u at 150 K, before a very drastic broadening to a maximum width of $\sim$ 0.08 r.l.u at a temperature of 165 K. Similar behaviours can be observed for both the $(0.676, 0.676, 0)$ and $(0.676, 0.676, 2)$ magnetic Bragg peaks, in every case, between temperatures of 2 K and 140 K, the widths can be seen to remain near constant. Following this, at

150 K, a very clear broadening can then be observed.

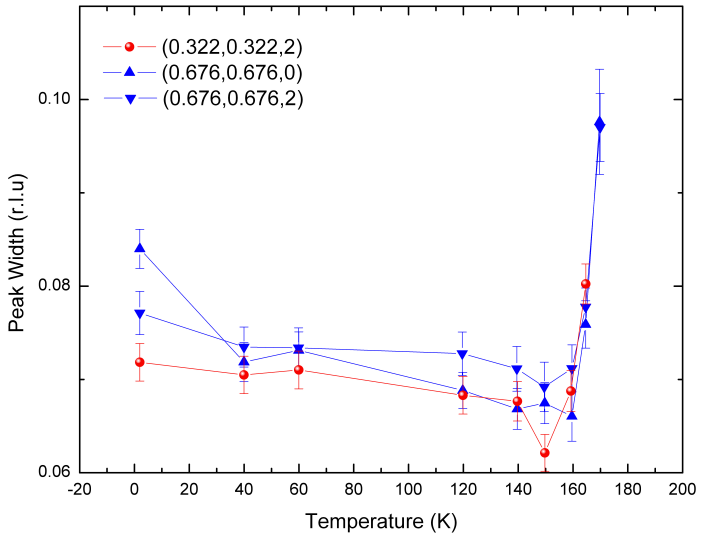

Figure 3.16: The temperature evolution of the Out-of-Ni-O-plane peak widths on first warming for l = even.

Reheating, l = odd

When studying the reheating data, out-of-Ni-O-plane, we first study the width of the $(0.322, 0.322, 3)$ magnetic Bragg peak. We observe that the peak broadens be 0.009 r.l.u between temperatures of 10 K and 20 K. However, following this, between temperatures of 20 K and 130 K, the width of the peak can be observed to stay more or less the same, with an approximate width of 0.045 r.l.u. Exceeding 130 K, the peak can be observed to suddenly and drastically sharpen before re-broadening above 150 K, to a width of $\sim$ 0.044 r.l.u at 160 K. Similar to the $(0.322, 0.322, 3)$ peak, the $(0.676, 0.676, 1)$ and $(0.676, 0.676, 3)$ magnetic Bragg peaks show a near constant peak width between 2 K and 130 K, which is followed by a clear sharpening at $\sim$ 140 - 150 K. Following this, in the case of all three magnetic Bragg peaks studied, a small amount of re-broadening can be observed beyond a temperature of

160 K.

On reheating, it is clear that the l = odd sees a sharpening with increasing temperature that is not observed on initial warming.

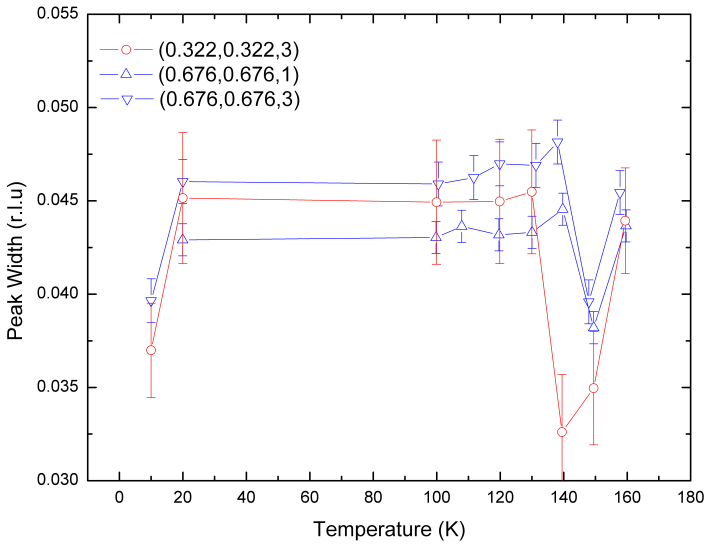

Figure 3.17: The temperature evolution of the Out-of-Ni-O-plane peak widths on reheating for l = odd.

Reheating, l = even

If we now study the the $(0.322, 0.322, 2)$ magnetic Bragg peak on reheating, we observe that between temperatures of 10 K and 20 K, the peak can be observed to broaden by approximately 0.004 r.l.u. Following this, between 20 K and 100 K, there is very little change to the width of the peak, holding at around 0.0755 r.l.u. At temperatures greater than 120 K, a gradual sharpening can be observed, until reaching a minimum width of 0.0625 r.l.u at a temperature of 150 K before a mild re-broadening to $\sim$ 0.0645 r.l.u at 160 K. We observe consistent behaviours with both the $(0.676, 0.676, 0)$ and $(0.676, 0.676, 2)$ peaks as the $(0.322, 0.322, 2)$ magnetic Bragg peak, in every case the peaks can be observed to broaden between 10 K and

20 K, which is followed by a region of constant width up to a temperature of 100 K. The peaks can then be observed to sharpen until reaching a temperature of 150 K, after which, a minor re-broadening can be observed.

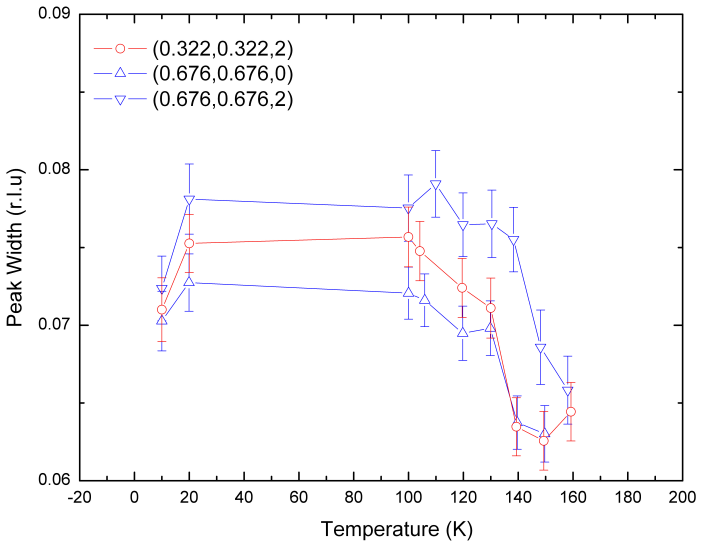

Figure 3.18: The temperature evolution of the Out-of-Ni-O-plane peak widths on reheating for l = even.

3.2.11 Averaging of Reheating Data out-of-Ni-O-plane

After doing so, both the l = odd and the l = even trends were averaged, such that a more accurate picture of what exactly was occurring could be seen, the warming and reheating data were overlain such that they could be directly compared. Doing so confirmed the same discrepancy as earlier described.

Following this, the l = odd and l = even warming data were overlain, and the same was done for the reheating data, showing that both the in the case of both the warming and reheating studies, the peaks show similar trends. This is due to both the l = even and l = odd being seen to sharpen on cooling, between temperatures of 150 K and 130 K. However, this is minimally more noticeable for the l = odd data.

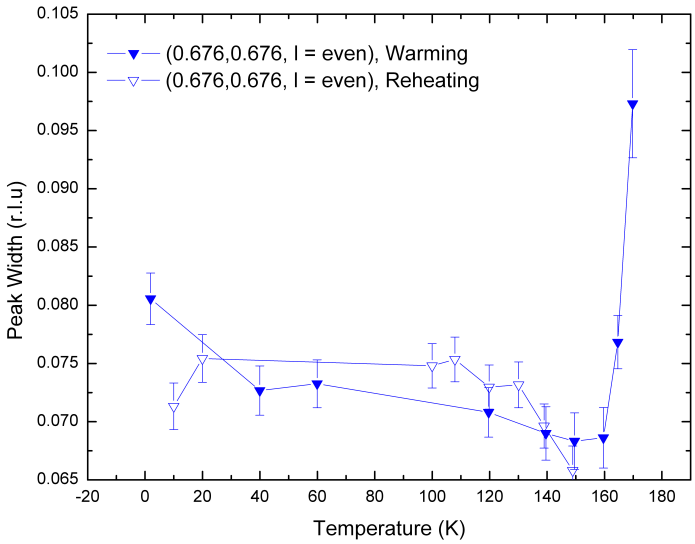

Figure 3.19: The temperature evolution of the peak widths for the l = even data on reheating after averaging.

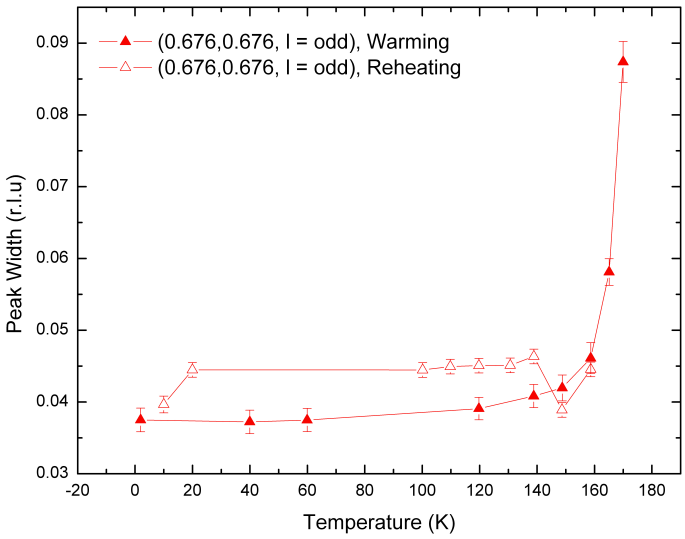

Figure 3.20: The temperature evolution of the peak widths for the l = odd data on reheating after averaging.

The reheating data also shares similarities between l = even and l = odd data.

In both cases, an increase in the peak widths can be observed between temperatures of 10 K and 20 K, followed by a region between 20 K and $\sim$ 130 K, were no real difference in peak widths can be observed for both l = odd and l = even. Beyond this, a small sharpening in both trends can be observed between 130 K and 150 K.

3.2.12 In-Plane Peak Widths

l = odd

If we now study the scan direction parallel to the in-plane direction, l = odd. If we study the $(0.322, 0.322, 3)$ magnetic Bragg peak, we observe that the peak width remains fairly constant between temperatures of 20 K and 140 K, around 0.0044 r.l.u. Following this the peak can be observed to slightly sharpen to a width of approximately 0.0033 r.l.u by 150 K. At a temperature of 160 K, the peak can be observed to have broadened to a maximum width of 0.013 r.l.u. by 180 K. We observe similar behaviour for both the $(0.676, 0.676, 1)$ and $(0.676, 0.676, 3)$ peaks. It should be noted that at higher temperatures, $>$ 160 K, there are some data points that no longer display consistent behaviour, this is the most apparent in the case of the $(0.676, 0.676, 1)$ magnetic Bragg peak.

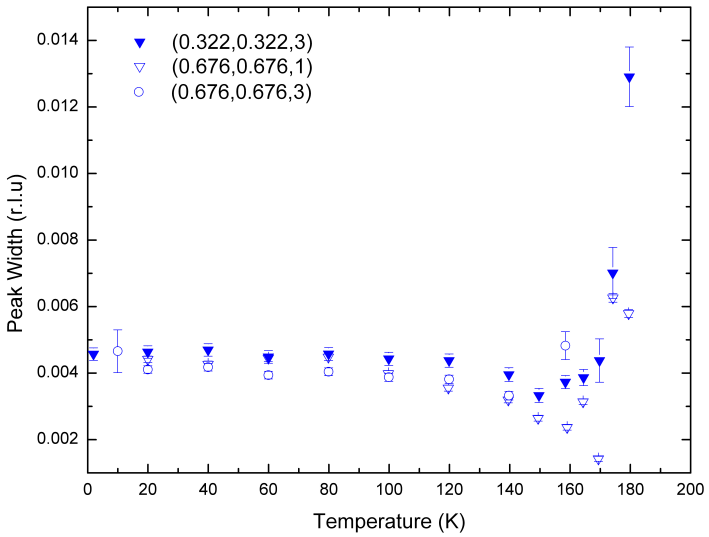

Figure 3.21: The temperature evolution of the In-Ni-O-plane peak widths for l = odd.

l = **even**

Now studying the scan direction parallel to the in-plane direction, l = even. Looking at the $(0.322, 0.322, 2)$ magnetic Bragg peak, we observe that the maintains a near constant width of ~ 0.00625 r.l.u between 2 K and 100 K, at which point, a mild sharpening occurs. At 165 K, further sharpening can be observed, were the width of the peak drops from 0.009 r.l.u to < 0.007 r.l.u. Exceeding a temperature of 165 K, when the peak is its sharpest, a re-broadening can be observed until reaching a maximum width of ~ 0.0093 r.l.u at 180 K. Largely, both the $(0.676, 0.676, 0)$ and $(0.676, 0.676, 2)$ magnetic Bragg peaks display behaviours consistent with that of the $(0.322, 0.322, 2)$ peak. This is the case until we reach a temperature of $\geq$ 165 K, at which point, the widths of all three peaks is no longer consistent with one another, this may be due to potential thermal fluctuations at these higher temperatures.

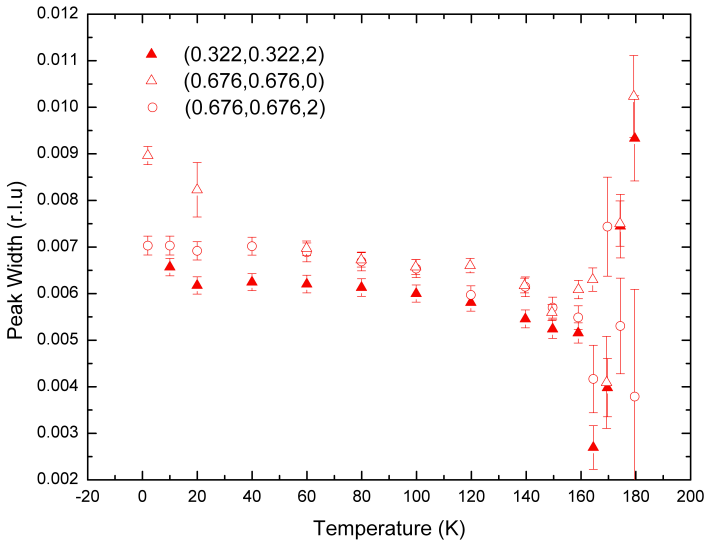

Figure 3.22: The temperature evolution of the in-Ni-O-plane peak widths for l = even.

3.2.13 Discussion of In-Plane Peak Widths

As with the out-of-plane peak widths, the in-plane peak widths can also be observed to sharpen on warming. However, unlike the out-of-plane direction, the in-plane peak widths have comparable sharpening for both l = odd and l = even, not only l = even. Despite this sharpening being observed in the $x = 0.275$ sample, it was significantly less than that of the out-of-plane sharpening and as so, was believed to be an artefact of this significant out-of-plane sharpening on warming.[3] However, this is not the case with the $x = 0.37$ sample as the sharpening is observed for the l = odd peaks scanned in-plane, but not out-of-plane. This would suggest that the in-plane sharpening is an intrinsic effect, rather than an artefact of the out-of-plane sharpening, as previously thought.

3.2.14 Comparison of Anomalous Broadening of Magnetic Bragg Peaks in LSNO

Broadening Observed for LSNO $x = 0.275$

If we first study the temperature evolution of the widths of the magnetic Bragg peaks for $x = 0.275$, we observe an 'anomalous brodening' of the magnetic Bragg peaks as a function of cooling. Along the out-of-Ni-O-plane scan direction, the Bragg peaks can be observed to broaden on cooling below temperatures of 110 K. This is far more apparent for $l =$ even than $l =$ odd. An in-Ni-O-plane broadening is also observed, and was thought to be an artefact of the significant out-of-Ni-O-plane broadening.[3] Below this temperature, it is thought that as the magnetic order becomes better established, it competes with the charge-ordered interactions, i.e. the magnetic order introduces disorder to the charge-order, this is known as a 'disorder by order' mechanism. It is thought that this mechanism drives the broadening, as seen in $x = \frac{1}{3}$ near its spin-ordering temperature,[4] where the incommensurability is already at its base temperature value.

If we compare the earlier findings relating to the broadening of the peak widths on cooling to $x = 0.275$, we see a similarly anomalous broadening both in and out-of-Ni-O-plane scan directions. In the case of the $x = 0.275$ sample, the broadening is calculated between temperatures of $\sim$ 110 K and 2 K, where 110 K is near the calculated corner temperature. This is further supported by the work of *Freeman et. al, 2010,*[3] who report that for that the width of the $l =$ odd peak stays near constant up to 110 K, beyond which, the peak can be observed to broaden when approaching the T_{SO}.

Studying the out-of-Ni-O-plane peak widths for $x = 0.275$ sample, we observe a very significant broadening of $58.6 \pm 2.0\%$ for $l =$ even. Conversely, we observe a small amount of broadening for the $l =$ odd peaks, seen in Figure 3.23. However, When studying the in-Ni-O-plane peak widths of the $x = 0.275$ sample, we observe

less broadening for l = odd than for the in-plane case, of $11.0 \pm 0.4\%$ for l = even and a broadening of $3.2 \pm 0.2\%$ for l = odd, as seen in Figure 3.24.

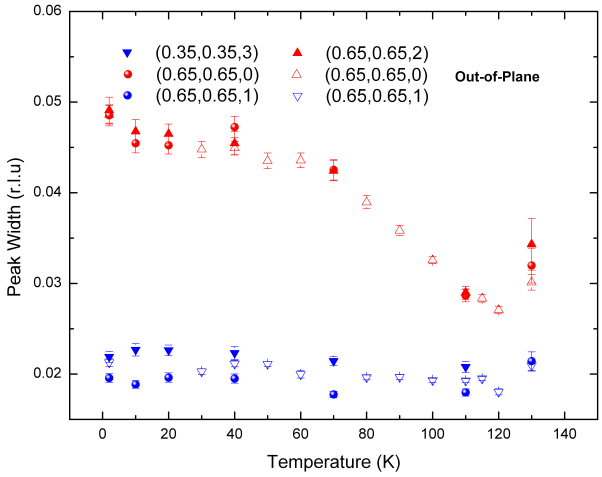

Figure 3.23: The temperature evolution of the Out-of-Ni-O-plane peak widths, LSNO $x = 0.275$, highlighting the broadening on cooling.

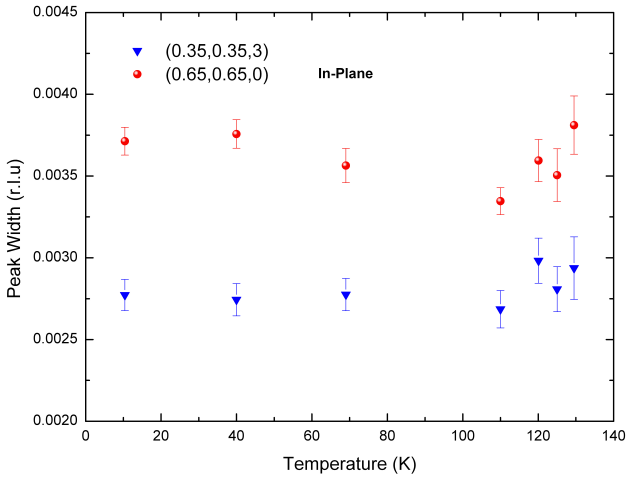

Figure 3.24: The temperature evolution of the in-Ni-O-plane peak widths, LSNO $x = 0.275$, highlighting the broadening on cooling.

We can clearly see from Figure 3.23, that the broadening on cooling is the most significant between temperatures of 110 K and 70 K. This shows an agreement with

the corner temperature calculated from the incommensurability, 112.72 ± 0.21 K, and as so would suggest that in the case of the $x = 0.275$ sample, that the incommensurability is in fact linked to the anomalous broadening on cooling.

Broadening Observed for LSNO $x = 0.37$

We observe an similar broadening of the magnetic Bragg peaks studied in $x = 0.37$, on cooling below temperatures of $\sim$ 160 K. Out-of-Ni-O-plane only the l = even peaks can be observe to broaden on cooling. However, in-Ni-O-plane both the l = even and the l = odd peaks can be observed to broaden.

For the out-of-Ni-O-plane data, the l = even peak can be observed to broaden by $15.0 \pm 0.6\%$ on cooling between 160 K and 2 K. When studying the in-plane data, we observe a broadening of $19.8 \pm 1.0\%$ for l = even and a broadening of $24.3 \pm 1.6\%$ for l = odd.

The fact that the broadening in-plane is larger than that of the broadening observed out-of-plane in $x = 0.37$, again suggests that the in-plane broadening is an intrisic effect and not an artefact of the significant out-of-plane broadening as was thought with $x = 0.275$.[3]

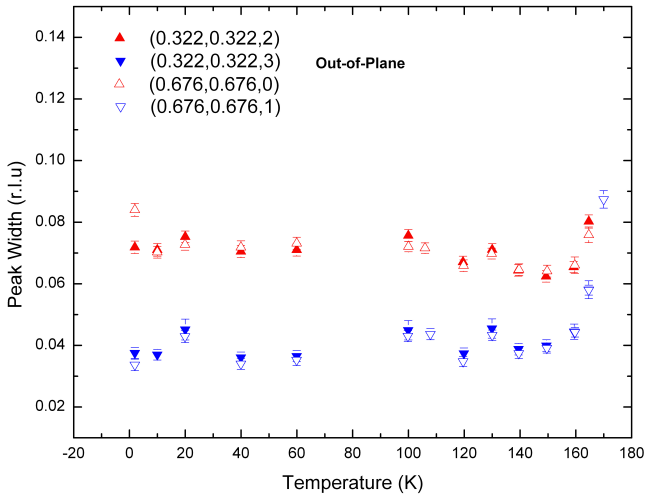

Figure 3.25: The temperature evolution of the Out-of-Ni-O-plane peak widths, LSNO $x = 0.37$, highlighting the broadening on cooling.

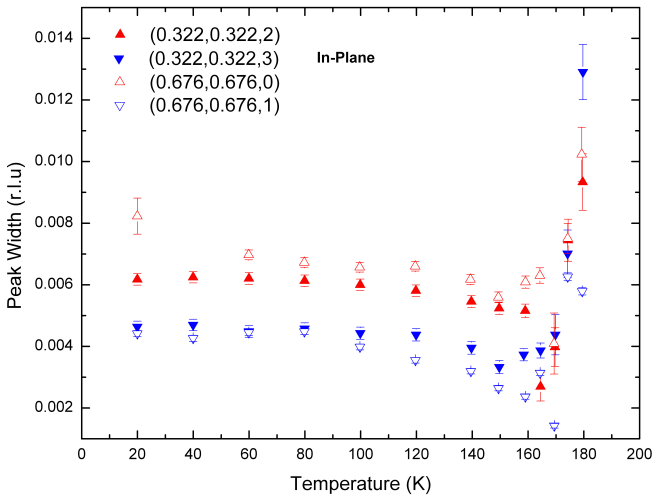

Figure 3.26: The temperature evolution of the in-Ni-O-plane peak widths, LSNO $x = 0.37$, highlighting the broadening on cooling.

3.2.15 Anomalous Broadening Observed in Reheating Study

When studying the percentage broadening of the original warming, $l = 2$ data were used for both the low and high **Q** peaks. Ideally, for the high **Q** peak, $l = 0$ should

be used for consistency. However, the width of this peak at 2 K appears significantly larger than originally anticipated and may be subject to further analysis. In doing so, we calculate a broadening of $4.5 \pm 0.2\%$ for the low **Q** peak and a broadening of $10.7 \pm 0.4\%$ for the high **Q** peak on cooling for the original warming data.

If we now calculate the broadening observed for the reheating data, we observe more familiar broadenings of $10.2 \pm 0.4\%$ for the low **Q** peak and $11.5 \pm 0.5\%$ for the high **Q** peak. It should be noted that due to the high **Q** peak having issues with the $l = 0$ data at 2 K, the $l = 2$ data were instead used, this presented another problem as no data were recorded at 2 K for $l = 2$, the closest measurement was made at a temperature of 10 K, and so for the high **Q** peak, there is a potential for further broadening on cooling to 2 K.

As the percentage broadening seen on cooling is similar for both overall broadenings, where the warming and reheating data were merged, and the broadenings observed in the reheating data are similar, we can conclude that the reheating of the sample has had the largest impact on the broadening of the peak widths and, as so has had the largest influence on the reduction of the magnetic correlation lengths.

3.2.16 Broadening Ratios

If we now compare the ratios between the widths of $l =$ even and $l =$ odd for both doping levels at base temperature as well as at that doping levels corner temperature, we observe some similarities. For the $x = 0.275$ sample, we observe that at base temperature, the $l =$ even peaks are again approximately 2.2 broader than that of the $l =$ odd peaks. Similarly, if we study the $x = 0.37$ sample, we observe that at base temperature the $l =$ even peaks are again a factor of ~ 2.2 broader than that of the $l =$ odd peaks. At the respective corner temperatures, we observe that the $l =$ even peaks are around 1.4 times larger than the $l =$ odd peaks for the $x = 0.275$ sample, while the peaks in the $l =$ even peaks in the $x = 0.37$ sample are a factor

of $\sim$ 1.5 larger than the l = odd peaks. From this, it can be observed that the broadening ratios for both the $x = 0.275$ and $x = 0.37$ samples is the same.

3.2.17 Correlation Lengths in $x = 0.37$

From the earlier dubbed, anomalous broadening seen in both $x = 0.37$ and $x = 0.275$, we would expect to see a reduction in correlation length, it is expected for samples such as this, that they would be relatively well correlated, with correlation lengths of 100 Å or greater.[3]

From the corrected peak widths, the correlation lengths of both the in-Ni-O-plane and out-of-Ni-O-plane can be determined. Due to the variable lattice parameters, due to the sample being a body-centred tetragonal lattice, (B.C.T), and the directionality of the charge-stripe formation, the correlation lengths for both of these planes required different formulae for their calculation. In order to calculate the in-Ni-O-plane correlation length, the following must be used:

$$\text{in-plane Correlation Length} = \frac{1}{(\frac{2\pi}{a})\sqrt{2}\sigma_{int}}$$

As with earlier, a refers to the lattice parameter of the ab plane of the tetragonal structure, which in the case of the $x = 0.37$ sample is 3.83 Å. $\sqrt{2}$ is used as the charge-stripes form along the diagonals of the samples ab plane.[5] In doing so, in-Ni-O-plane correlation lengths in excess of 100 Å were calculated, thus agreeing with previous observations.[1]

The out-of-Ni-O-plane correlation length is slightly different and given by use of the following formula:

$$\text{Out-Of-Plane Correlation Length} = \frac{1}{(\frac{2\pi}{c})\sigma_{int}}$$

c refers to the lattice parameter, which in the case of the sample used is 2.72 Å. By application of the above formula, out-of-Ni-O-plane correlation lengths of 28.5 ± 0.81Å for l = even peaks and 55.5 ± 2.8Å for l = odd peaks were calculated,

this is to be expected as it has previously been observed that the correlation lengths for l = odd and l = even differ by a factor of ≈ 2.[1]

The correlation lengths of the magnetic order in the $x = 0.37$ sample had previously been calculated by *Fremman et. al, 2004*. After discussion with *Freeman*, on this different correlation lengths determined in the earlier, lower resolution study, the correlation lengths determined in this work are agreed to be the most accurate.[7]

3.2.18 Discussion of Elastic Neutron Scattering Study

From the temperature evolution studies above, there is no clear correlation between the corner temperature and the broadening of the magnetic Bragg peak widths on cooling. This leads us to conclude that the temperature evolution of the incommensurability, though linked to the broadening in the $x = 0.275$ sample, does not appear to be directly linked to the broadening of the magnetic Bragg peaks observed in the $x = 0.37$ sample.

The magnetic ordering processes in $x = 0.37$ appears to be more complex than that of the $x = 0.275$. This complexity relates to the fact that the holes in the valence band of the overdoped sample disrupt the ordering of the sample. Whereas, in the underdoped regime, the sample is capable of self-doping, in turn introducing more holes, in order to achieve optimal stability seen at $x = \frac{1}{3}$.

3.3 Transitions from Magnetization Data

The magnetization of both LSNO $x = 0.275$ and LSNO $x = 0.37$ have been plotted as a function of temperature, such that confidence in the corner temperature, as determined in the incommensurability section, could be gained. $\frac{dM}{dT}$ was then plotted as a function of temperature, as it is believed from the works of *Giblin et. al, 2008*, that all the magnetic transitions can be observed by studying this data.[6] When the

magnetization observes a transition, it does so on a static timescale, meaning that the transitions observed are real.

The applied magnetic field, **H**, was orientated to be parallel to the growth axis, which is approximately $[1, 1, 0]$. Both of the single crystal samples were cooled in a magnetic field, with a strength of 500 Oe, while cooling.

The magnetization of both the $x = 0.275$ and $x = 0.37$ samples was recorded on a SQUID magnetometer, (Superconducting Quantum Interference Device). SQUID magnetometers are one of the most sensitive techniques for measuring magnetic properties. Magnetometers can readily determine the bulk net magnetic moment of materials. It should be noted that for antiferromagnetic samples, the magnetization is zero unless a magnetic field is applied to the sample.[8]

A magnetic sample is placed in an applied magnetic field, that induces a net magnetization in the sample. As the sample is moved up and down through the detection coils, magnetic flux lines from the sample induce a superconducting current in the superconducting detection coils, which is recorded by the detector. From variations in the detected signal to sample position is converted to the sample net magnetization by comparison to a calibrated scale, obtained by measuring known magnetic standards.[9]

A SQUID ring with a 'weak link', which consists of two superconductors which are separated by a thin layer of insulator, in doing so two parallel Josephson Junctions are formed. The electrical current density through these weak links, between he two superconductors, is dependent on the phase difference, $\Delta\phi$, of the two superconductors wave-functions. The time derivative of the phase difference, $\frac{d\Delta\phi}{dt}$, relates to the voltage across this weak contact. Further to this, the $\Delta\phi$ is influenced by the magnetic flux, Φ, through the rings. As such, a SQUID can be used to convert magnetic flux into a voltage. In a SQUID magnetometer, the detection coils are made up of superconducting wire and along with the SQUID antenna are responsible for

transferring the flux to the SQUID detector, which converts the magnetic flux to an electrical voltage, which is converted into the net magnetization of the sample.[8,9]

3.3.1 Determining Transitions from Magnetization Data for LSNO $x = 0.275$

If we first study the magnetization of the LSNO $x = 0.275$ sample from a previous study when cooled in a magnetic field, (FC), we observe three distinct features, these being: the spin-reordering temperature, T_{SR}, the spin-ordering temperature, T_{SO}, and the charge-ordering temperature, T_{CO}, all of which are clearly labelled and occur at temperatures of approximately 5 $\pm$ 2.5 K, 135 $\pm$ 2.5 K and 152.5 $\pm$ 2.5 K respectively. The T_{SO} and T_{CO} have previously been determined for this doping level, these are 140 $\pm$ 5 K[3] and 160 $\pm$ 10 K[10] respectively and so, our findings are consistent with these results.

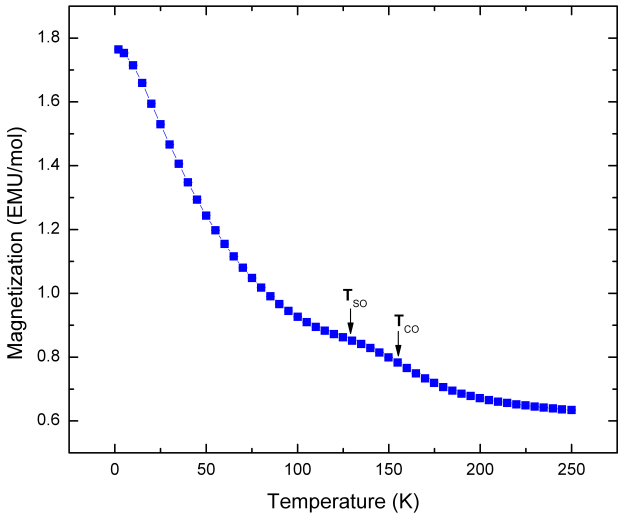

Figure 3.27: The temperature evolution of the FC magnetization of LSNO $x = 0.275$.

The gradient of this data was then plotted as a function of temperature such that as with the incommensurability data, the corner temperature of the sample could

be determined. This was again done by taking two linear temperature regions and equating the equations of the fits and solving simultaneous equations for the point of intersection.

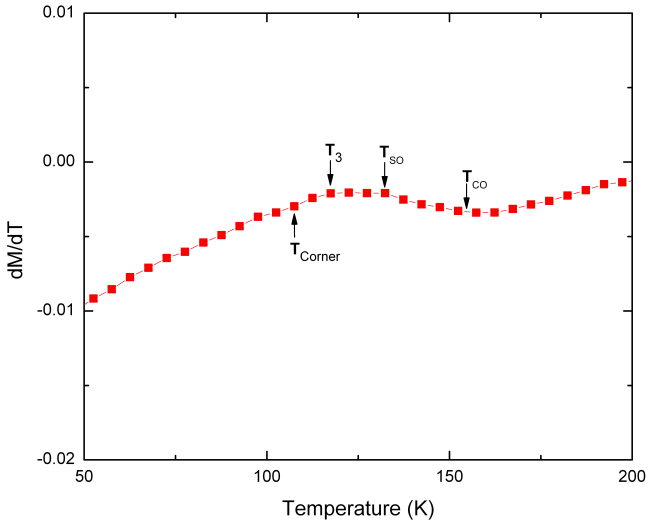

Figure 3.28: The temperature evolution of dM/dT of FC data of LSNO $x = 0.275$.

The temperature ranges elected for use were between 25 K - 100 K and 150 K - 195 K, as at these temperatures there does not appear to be any potential ordering processes as the data appears to be near linear. From each of these linear fits, an equation was provided by the plotting software. Both of these equations could be solved by making use of simultaneous equations and solving for the corner temperature, which was found to be 113.9 ± 2.5 K in this case.

The corner temperature using the incommensurability of this data verifies this, as the corner temperature calculated from that study was 112.7 ± 5.6 K. The small disagreement could again be ascribed to the use of the sample being studied with two different thermometers.

3.3.2 Determining Transitions from Magnetization Data for LSNO $x = 0.37$

Now looking at the magnetization of the LSNO $x = 0.37$ sample when cooled in a magnetic field, (FC), we again see the T_{SR}, T_{SO} and T_{CO}. All of these ordering processes occur at slightly higher temperatures in this sample than in the $x = 0.275$ sample, occuring at temperatures of 7.5 ± 2.5 K, 177.5 ± 2.5 K and 237.5 ± 2.5 K respectively. Both the T_{SO} and T_{CO} have previously been determined for this doping level, these are 170 ± 5 K and 230 ± 10 K respectively[1] and so, our findings are consistent with these results.

The gradient of this plot was once again plotted as a function of temperature such that two linear temperature regions could be obtained such that the corner temperature could be calculated from the equations of the linear fits.

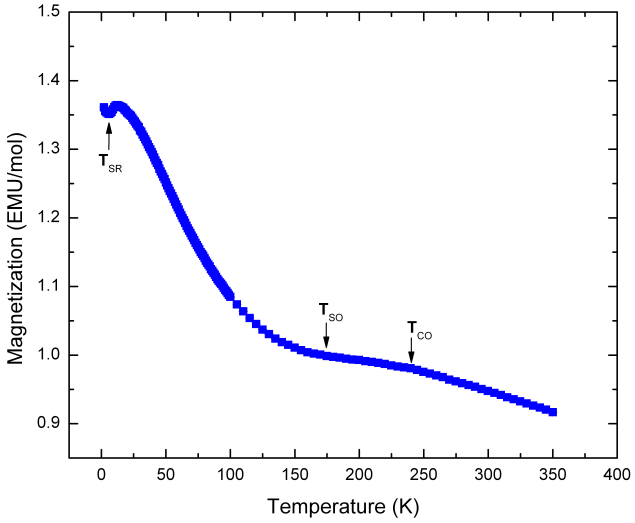

Figure 3.29: The temperature evolution of the FC magnetization of LSNO $x = 0.37$.

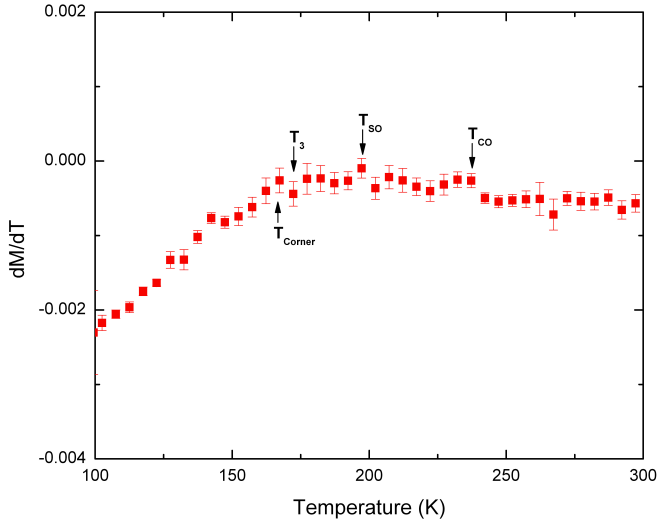

Figure 3.30: The temperature evolution of dM/dT of FC data of LSNO $x = 0.37$.

The temperature ranges elected for use were between 60 K - 140 K and 170 K - 235 K, as at these temperatures there does not appear to be any potential ordering processes as the data appears to be near linear. From each of these linear

fits, an equation was provided by the plotting software. Both of these equations could be solved by making use of simultaneous equations and solving for the corner temperature, which was found to be 161.4 ± 2.5 K in this case.

In the earlier study, relating to the incommensurability of the $x = 0.37$ sample, a corner temperature of 154.1 ± 4.4 K was calculated. Whilst, the corner temperature calculated from the magnetization data does not perfectly agree with this, it is reasonable to believe that the corner temperature lies somewhere within this region. This minor disagreement could be due to the samples being studied with two different thermometers or the fact that a different crystal was used.

3.3.3 Discussion of Transitions in Magnetization Data

In the case of the $x = 0.275$ sample, we find that the T_{SO} and T_{CO} determined from the magentization data agree with previous work. For the $x = 0.37$, while the T_{SO} and T_{CO} determined from the magentization data agree with previous results, the transitions appear to occur at slightly higher temperatures, although this can likely be attributed to potential differences in the $x = 0.37$ samples used.

As the values of both the T_{SO} and T_{CO} agree with findings made in previous work, we believe that the data marked as T_3 in Figures 3.28 and 3.31 can be thought of as an onset to the transition that occurs at the corner temperature. This is due to the fact that in both cases T_3 occurs at slightly higher temperatures than the transition that occurs at the corner temperature.

Chapter 4

Results of Magnetic Excitations

In this chapter, the observation of quasi-one-dimensional excitations will be discussed as well as their temperature dependence. The magnetic excitations induced via inelastic neutron scattering will also be studied in such a way that any offset between the magnetic Bragg peak centres and the magnetic excitation peak centres is apparent at the lowest energy transfers.

CHAPTER 4

4.1 Example of Data Produced by Inelastic Neutron Scattering

The inelastic neutron scattering data typically presents itself in the following form when plotted:

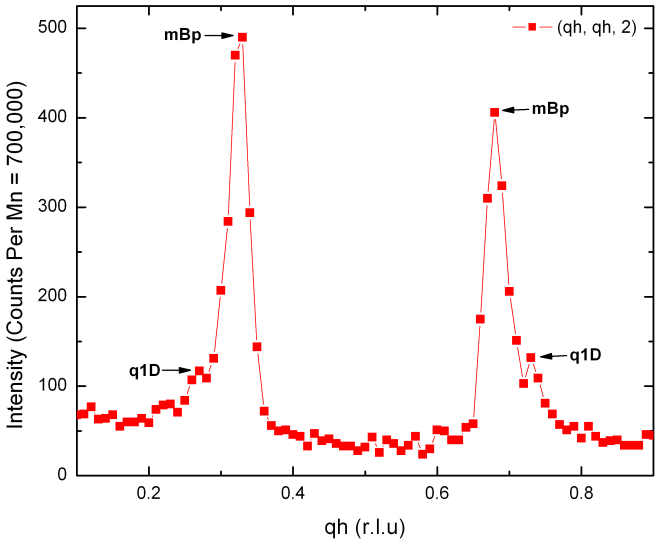

Figure 4.1: A typical plot showing magnetic Bragg peaks produced by inelastic neutron scattering along the (h, h, l) scan direction for $l = 2$ at a temperature of 20 K.

As with the elastic neutron scattering data, peaks are typically centred on $((\frac{h\pm\varepsilon}{2}), (\frac{k\pm\varepsilon}{2}), l)$ due to the magnetic ordering in the charge-stripe ordered phase. The intensity of the peaks is far less than that of the magnetic Bragg reflections, due to the lower probability of a neutron creating a spin excitation.

4.2 Quasi-One-Dimensional Excitation

Upon studying the magnetic excitations of the LSNO $x = 0.37$, a 'shoulder' of sorts can be observed near both of the magnetic Bragg peaks,[1] and can be seen in the

Figure 4.1. This is apparent in the case of the 2 K measurement, with a excitation of energy 1.5 meV. Previously, this excitation was shown to be from quasi-one-dimensional magnetic excitations of the charge-stripe electrons, q-1D,[1] and so, the temperature evolution of this excitation must be investigated.

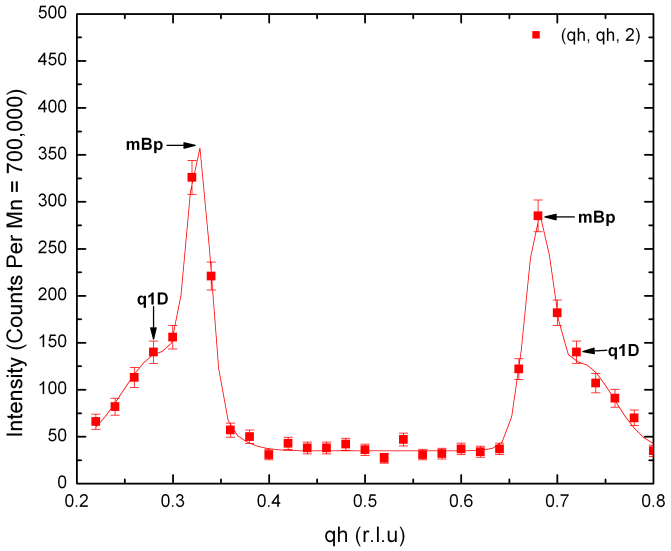

Figure 4.2: A typical plot showing magnetic excitations from the magnetically ordered spins and q-1D magnetic excitations produced by inelastic neutron scattering, from a scan measured along the (h, h, l) scan direction for $l = 2$ at a temperature of 2 K.

The temperature evolution of the q-1D excitations was investigated by studying all excitations induced by neutrons of energy 1.5 meV and recording both the widths and the centre position of both the magnetic excitation and magnetic Bragg peak centres. In order to accurately do so, each of the data were broken up into low, > 0.5 r.l.u, and high $\mathbf{Q}$, < 0.5 r.l.u, text files, such that the necessary excitations could be compared to the nearest magnetic Bragg peak.

All of the data was fitted with two Gaussian peaks, the temperature evolution of the position of both the low $\mathbf{Q}$ magnetic excitation and magnetic Bragg peaks were plotted and from this, it can be seen that the magnetic excitation kinks to

track the magnetic Bragg peak upon warming, as expected theoretically.[2] This is a fairly consistent tracking between temperatures of 2 K and 60 K. However, for temperatures of 60 K and above, we observe that the q-1D is no longer tracking the changing magnetic structure.

The temperature evolution of the position of the peak centre of the high **Q** magnetic excitation and magnetic Bragg peaks were then plotted. This showed similar behaviours upon warming, the position of the peak centre begins to track the magnetic Bragg peaks between 20 K and 60 K. However, similarly to the low **Q** data, stops tracking the changing magnetic order beyond a temperature of 60 K.

The fit of all free parameters proved to be unstable and as so, the parameters that would otherwise determine both the width and the centre position of the q-1D magnetic excitation had to be fixed in place before plotting. They were fixed such that they would maintain both the same position as the q-1D excitation at a temperature of 20 K. In the plotting process, it was observed that the best quality fits for data between temperatures of 20 K and 120 K were provided by fitting a Gaussian line shape. In the case of the low **Q** excitation, the position of the excitation centre was set to 0.27 r.l.u, whilst the high **Q** was set to 0.73 r.l.u. In the case of both peaks, the width was constrained to 0.01 r.l.u, as this was the smallest interval in all the data used for these plots.

After constraining this data, to further confirm that the q-1D was no longer present, 1.5 meV excitation data at 80 K. was plotted to see if it is visible if plotted, this can be seen in the below Figure 4.3.

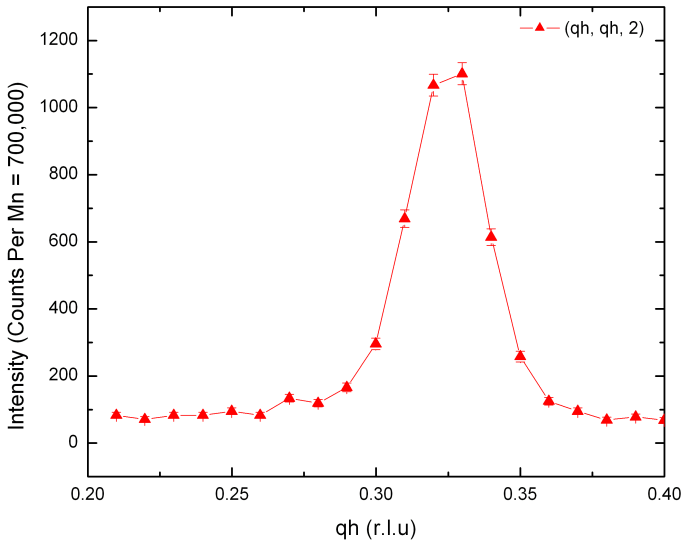

Figure 4.3: Figure displays how the q-1D magnetic excitation is no longer visible by a temperature of 80 K. For clarity, the region where we would expect the q-1D to be visible, between 0.2 r.l.u - 0.4 r.l.u has been focused on.

As we can see, by a temperature of 80 K, the q-1D can no longer be observed, so the integrated intensity of the q-1D will now be investigated to confirm that this is, in fact the case. As discussed in the works of *Freeman et. al, 2008*, the integrated intensity of the q-1D magnetic excitations in LSNO $x = \frac{1}{3}$ drastically decrease with increasing temperature and are practically non-existent beyond a temperature of 120 K.[3] The integrated intensity of the q-1D magnetic excitation for LSNO $x = 0.37$ sample was then plotted, as seen in Figure 4.4.

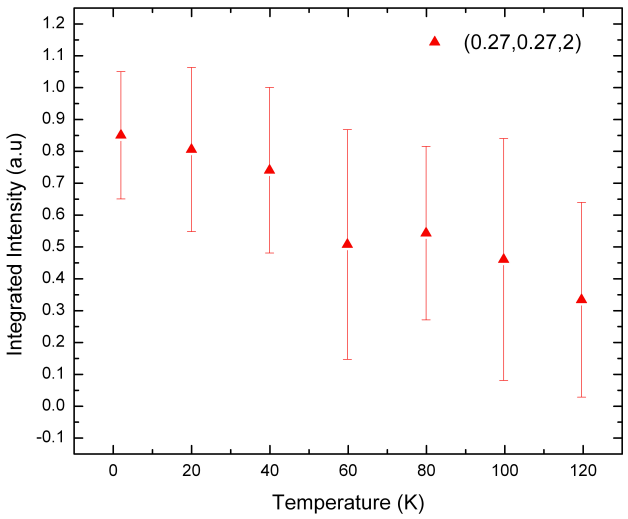

Figure 4.4: The integrated intensity of the q-1D magnetic excitation centre near $(0.322, 0.322, 2)$ as a function of temperature.

From plotting the integrated intensity as a function of temperature, we can see that the intensity of the q-1D is near zero at a temperature of 80 K and as so, is consistent with the findings made by *Freeman et. al, 2008* in LSNO $x = \frac{1}{3}$.[3]

4.3 Magnetic Excitations

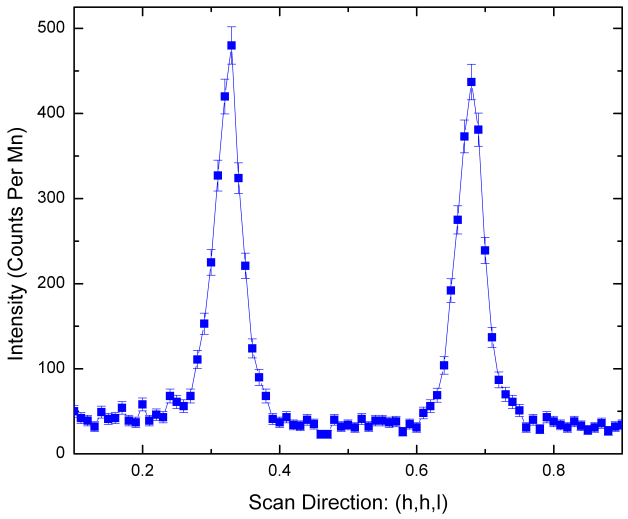

Figure 4.5: A typical plot showing magnetic excitation peaks produced by neutron loss scattering, 3.5 meV, along the (h, h, l) scan direction for $l = 2$ at a temperature of 180 K.

The magnetic excitations were then studied, such that any offset between the wave vector centring of both the magnetic Bragg peaks and the magnetic excitation peak centres could be clearly seen. This was done for both the low **Q** and high **Q** peak centres along the in-Ni-O-plane scan direction. These excitations were induced by means of neutron loss scattering, a technique where a fraction of the kinetic energy of the incident neutron is transferred to the sample, and so, the kinetic energy of the scattered neutron is sufficiently less than that of the incident neutron, thus making this process inelastic.

In order to study the lowest energy transfers, 'cold' neutrons were used as 'thermal' or 'hot' neutrons would be unable to study excitations at such low energies. 'Cold' refers to the kinetic energy of the neutron, which is determined by the medium which moderates the neutrons, likely liquid deuterium in this case. Neutrons such as this have kinetic energies in the range of 0 meV - 250 meV.[4] The energies of the

neutrons used to induce excitations in this study ranged between 0.6 and 4 meV.

These excitations were studied at two temperatures in two samples, LSNO $n_h = 0.22$ as well as LSNO $x = 0.37$. This was done such that, the point at which the magnetic excitations no longer to track the changing magnetic order would be obvious, as we would otherwise expect the magnetic excitations to behave as Nambu-Goldstone modes.[2]

If we first study the magnetic excitations observed in the LSNO $n_h = 0.22$ sample, studied at temperatures of 60 K and 120 K, we observe an offset between the wave vector centring of both the magnetic Bragg and magnetic excitation peak centres. Further to this, we also observe that the magnetic excitations in this sample, with energies of ≥ 3 meV appear to be unaffected by the changing periodicity of the magnetic order near the T_{SO}.

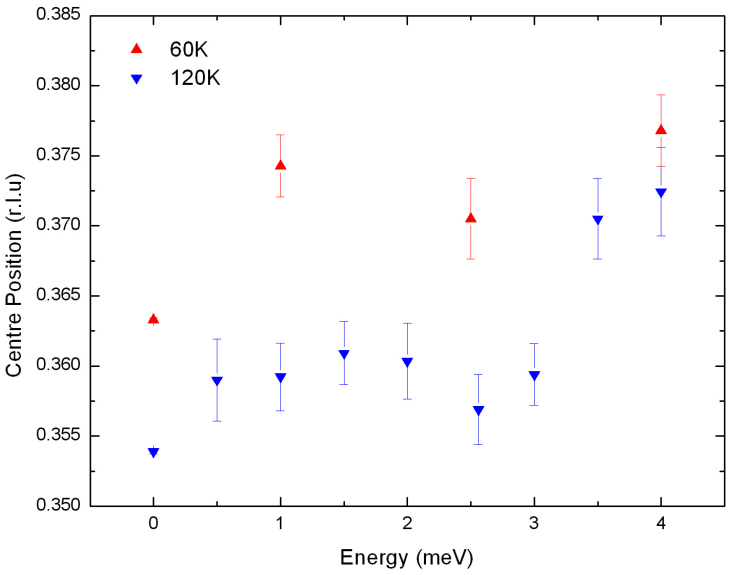

Figure 4.6: The position of the excitation peak centre as a function of energy for the excitation centred near (0.365,0.365,0) in LSNO $n_h = 0.22$.

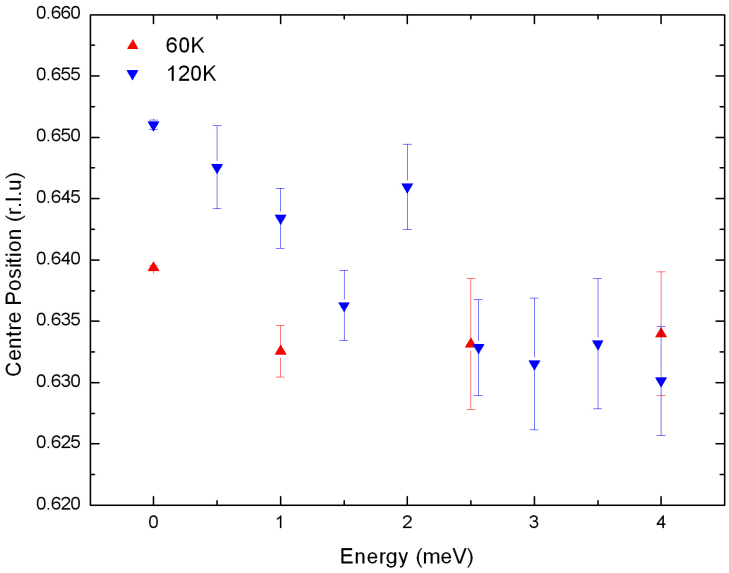

Figure 4.7: The position of the excitation peak centre as a function of energy for the excitation centred near (0.635,0.635,0) in LSNO $n_h = 0.22$.

We now turn our attention to the magnetic excitations observed in the $x = 0.37$ sample, studied at temperatures of 120 K and 180 K. We observe, that unlike the $n_h = 0.22$ sample, there is no offset between the wave vector centring of the magnetic Bragg and magnetic excitation peak centres. However, in a similar fashion to that of the $n_h = 0.22$ sample, it can once again be observed that the excitations in this sample with energies of 3 meV or greater, appear unaffected by the changing periodicity of the magnetic order near the T_{SO} and as so do not kink to track the changing magnetic structure at these energies.

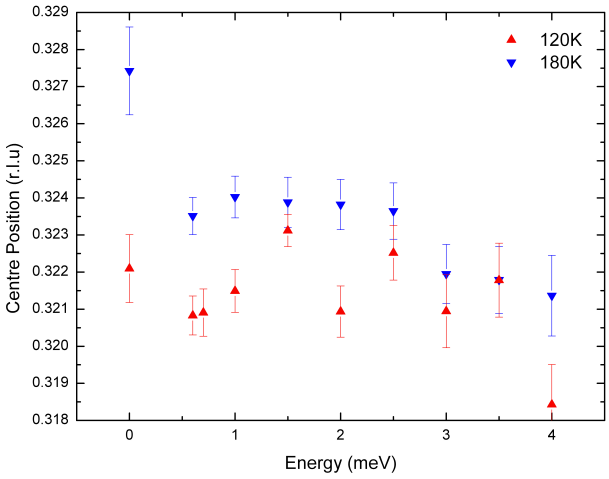

Figure 4.8: The position of the excitation peak centre as a function of energy for the excitation centred near (0.324,0.324,2) in LSNO $x = 0.37$.

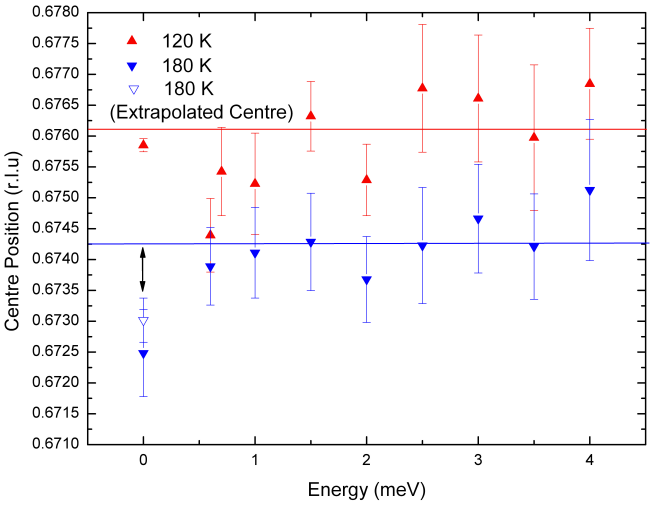

Figure 4.9: The position of the magnetic excitation peak centre as a function of energy for the magnetic excitation centred near (0.676,0.676,2) in LSNO $x = 0.37$. The lines should act as a guide to show any offset between the magnetic Bragg peak centres and the magnetic excitation peak centres. The open blue triangle is the centre of the magnetic Bragg peak extrapolated from the mgnetic Bragg peak centre positions between 160 K and 175 K.

As the magnetic excitations with energies of 3 meV or greater do not appear to

kink to track the changing periodicity of the magnetic order in either of the doping levels investigated in this study, we propose that the magnetic excitations at low energy transfers in the $x = 0.37$ sample display behaviour consistent with that of those observed in the $n_h = 0.22$ sample.

4.3.1 Corrections to Magnetic Excitations

As there exists a small offset between the magnetic Bragg peaks, as as seen in the case of the low and high **Q** peak centre positions for the LSNO $x = 0.37$ sample, a correction must first be applied. This requires that a ratio first be calculated between the magnetic Bragg peak and the 1.5 meV, inelastic data. In both cases, this was done for the inelastic peak centres at an average temperature of ~ 100 K. This is due to this point being believed to be a good indicator of where the excitation is truly centred, this ratio was then applied to all of the inelastic data.

The offset observed is likely due to an issue with the alignment of the sample, such as the wavelength of the instrument being incorrect or the sample not being fully centred within the beam. The wavelength is calibrated for by a collimated neutron beam for a wavelength used for diffraction without an analyser. An analyser is later installed and energy aligned. So it is likely that the wavelength for diffraction is correct.

Chapter 5

Conclusions

In this thesis, both the magnetic ordering processes and the magnetic excitations in $La_{2-x}Sr_xNiO_4$, $x = 0.37$ and $x = 0.275$, have been studied. In the case of the magnetic ordering study, the temperature evolution of both the incommensurability and the magnetic Bragg peak widths was studied. The response of the magnetic excitations to the changing incommensurability of LSNO was also studied in detail.

From previous work, performed by *Ishizaka et. al., 2004* and *Yoshizawa et. al., 2000*,[1,2] it was understood that LSNO is the most stable at $x = \frac{1}{3}$. From the group's work into the temperature evolution of the incommensurability of the material, it is understood that with increasing temperature the incommensurability of an LSNO sample will tend to a value of one third, correspond to charge-stripes spaced 3 Ni-Ni sites apart.

In order to determine the temperature evolution of the incommensurability for the doping levels used in this study, a fitting function was fitted to the data to determine the position of the magnetic Bragg peak centres. From this, the temperature evolution of the magnetic Bragg peak centres were determined. We observe that there are two temperature ranges for the incommensurability. The first, where the the incommensurability does not appear to vary with changing temperature, and another at higher temperatures where the incommensurability can be observed to

vary with temperature.

From these two regimes, a corner temperature could be calculated. The corner temperature is the temperature at which the incommensurability of the sample changes between the two regimes, this was determined from the incommensurability at temperatures away from this transition, determined for both doping levels. A corner temperature of 112.7 ± 5.6 K was calculated for the $x = 0.275$ sample, while 154.1 ± 4.4 K was calculated for the $x = 0.37$ sample.

When studying the temperature evolution of the widths of the Bragg peaks for the $x = 0.37$ sample, we observed that the point at which broadening on cooling, occurs at a lower temperature than the corner temperature calculated from the incommensurability data. This would suggest that the incommensurability is not directly linked to the anomalous broadening of the peaks on cooling. However, the broadening and the incommensurability appear to be linked in the case of the $x = 0.275$ sample.

If we now address the different broadening observed out-of-Ni-O-plane measured on initial cooling, only the l = even peaks can be observed to broaden on cooling, in the $x = 0.37$ sample. In the case of the $x = 0.275$ sample, the out-of-plane broadening is significant, so significant in fact that the small broadening previously observed in-plane[3] was thought to be an artefact of the out-of-plane broadening. However, in-plane, we observed that on warming from the initial cooling that there is broadening for both l = odd and
l = even peaks for both the $x = 0.275$ and $x = 0.37$ samples. In the $x = 0.37$ sample, there is in-plane broadening for the l = odd peak but no out-of-plane broadening for the l = odd peak, and the broadening of the in-plane for the l = even peak being is as large as the broadening out-of-plane, meaning there is an in-plane effect.

The anomalous broadening on cooling, both in the in and out-of-plane directions, for both doping levels studied, indicates that the magnetic correlation lengths reduce

on cooling. This is not what we would otherwise expect, as the peaks would typically sharpen on cooling, as the magnetic order becomes established.

As we now know the in-plane broadening to be an intrinsic effect, we must consider what is the mechanism that drives this broadening. A potential reason for this broadening is that the magnetic order does not like the value of the incommensurability at a base temperature and potentially prefers $\varepsilon = x$,[1,2] as the magnetic order's preference acts a disordering effect, causing the broadening of the magnetic Bragg peaks in-plane.[2] In the case of the $x = 0.37$ sample, the magnetic order may prefer $\varepsilon = x$ in order to remove holes from the valence band, as discussed later.

As seen with the $x = \frac{1}{3}$ sample, the static magnetic order causes a 'disorder by order' effect on the out-of-plane charge-stripe order correlation length, and so it would appear that the magnetic order prefers being more two-dimensional.[2,4] In the $x = 0.275$ sample, the disordering effect brought about by the magnetic order occurs at approximately the corner temperature, and in the case of the $x = 0.37$ sample, below the corner temperature.

If we now consider the out-of-plane peak widths measured while reheating, the peaks are observed to broaden on cooling, for both the $l =$ odd and $l =$ even peaks. This would suggest that the cycling of the temperature has brought about a possible re-ordering or the magnetism in the charge-stripe ordered state that causes more disordering effects, including the $l =$ odd peaks. This is due to the magnetic order attempting to be more two-dimensional, in turn causing the broadening out-of-plane on cooling.[2,3]

This study suggests that the magnetic ordering processes of the $x = 0.37$ sample appear significantly more complex that that of the $x = 0.275$ sample. This is likely due to the fact that in the $x = 0.37$ sample, the excess holes from Sr doping, that are not involved in the charge-stripe order in the valence band disrupt the magnetic ordering. However, in the $x = 0.275$ sample, the electrons from self doping are likely

promoted out of the valence band and into an impurity state. The impurity states are likely caused by the introduction of the Sr into the material. This electron promotion in the $x = 0.275$ sample provides the necessary additional holes by self-doping to enable ε to be closer to one third than the chemical doping, x. As the material acts as a Mott insulator, the electrons in the valence band will be unable to be promoted to the conduction band as the energy gap is significant, as seen in Figure 5.1, so they are likely to be promoted to impurity states.

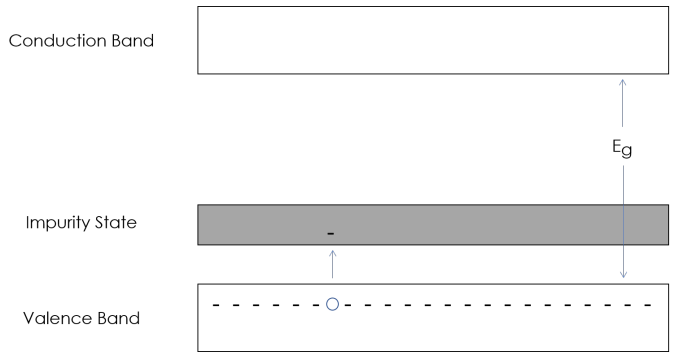

Figure 5.1: Figure shows how electron in the valence band may be promoted to the impurity state, leaving an additional hole in the valence band.

The magnetization of both of the afore mentioned samples was then studied as a function of increasing temperature. This was done such that any potential static effects, ie. phase transitions, could be observed. The magnetization appears to observe a subtle transition, suggestive of an ordered transition. However, the magnetization data does not determine exactly what the transition is, after finding the transitions, we propose, by comparing to neutron diffraction measurements, that they correspond to the charge ordering temperature and spin-ordering temperatures as observed by neutrons, and the corner temperature of the incommensurability. From this, we conclude that the corner temperature appears to be a phase transition. This required that the gradient of the magnetization be plotted as a function of temperature, as it is thought that all magnetic transitions can be observed in studying this data.[5] In doing so, there is a feature we have associated with the

corner temperatures of 113.9 ± 2.5 K for the $x = 0.275$ sample and 161.4 ± 2.5 K for the $x = 0.37$ sample. Any small disagreements that exist between the corner temperature calculations from the incommensurability data and the magnetization data could be due to the fact that different thermometers were used in each of these measurements, as well as different crystals being used.

In the magnetization data, transitions that appear to be the spin ordering temperature and charge ordering temperatures for both doping levels were determined. In the case of the $x = 0.275$ sample, a spin ordering temperature of 135 ± 2.5 K was calculated as well as a charge ordering temperature of 152.5 ± 2.5 K. For the $x = 0.37$ sample, as expected both of these ordering temperatures were slightly higher, with a spin ordering temperature of 177.5 ± 2.5 K and a charge ordering temperature of 237.5 ± 2.5 K being calculated.

When studying the magnetic excitations, we observe a quasi one-dimensional, antiferromagnetic, gapped excitation near both of the magnetic Bragg peaks. Upon studying the temperature evolution of this excitation, we believe that at temperatures of ~ 60 K and greater, that this excitation is no longer present. In doing so, it is clear that the behaviour of the q-1D magnetic excitation the $x = 0.37$ sample is consistent with that of the $x = \frac{1}{3}$ sample.[4] Further confirming that the q-1D excitation is doping independent in the C.S.O phase.

In both LSNO $n_h = 0.22$ and LSNO $x = 0.37$, it was expected that the magnetic excitations would track the changing periodicity of the magnetic order. For the $x = 0.37$ sample, the magnetic excitations from the magnetic order have the same wave vector and as so behave as Nambu-Goldstone Modes.[6] In the case of both samples investigated, the magnetic excitations induced by neutrons at energies < 3 meV appear to kink to track the changing magnetic structure as the incommensurability changes. However, the magnetic excitations induced by neutrons at energies ≥ 3 meV can no longer be observed to track the changing periodicity of

the magnetic order. This being the case, we can conclude that the behaviours of the magnetic excitations in response to the changing incommensurability, observed in the $x = 0.37$ sample, are consistent with those observed in the $n_h = 0.22$ sample.

To summarise, there appear to be many similarities in the magnetism of C.S.O materials, both above and below $\frac{1}{3}$ doping in the case of LSNO. We observe that in both cases the magnetic Bragg peaks can be observed to broaden on cooling, both in and out-of-plane. We also see that the magnetic excitations observed in both cases, induced by neutrons at energies < 3 meV appear to track the positions of the peak centres. There is a significant difference with doping in the magnetism of C.S.O LSNO, this is the fact that the incommensurability appears to be linked to the broadening in the $x = 0.275$ sample but not directly linked in the case of the $x = 0.37$ sample. In the case of the $x = 0.275$ sample, the broadening begins at approximately the corner temperature, but in the $x = 0.37$ sample, the broadening begins at temperatures lower than the calculated corner temperature.

To fully understand C.S.O in LSNO, we must be able to model the behaviours of the material at doping levels $< \frac{1}{3}$, $= \frac{1}{3}$ and $> \frac{1}{3}$. It is hoped that the work done in this thesis will provide further insight into our understanding of hole doped cuprates.

Appendix 1

Magnon Dispersion Relation for a Ferromagnet

The following derivations can be found in more detail in the works of *Blundell, 2014*.

Semi-Classical Approach

If we first consider the Hamiltonian operator for the Heisenberg model:

$$\hat{\mathcal{H}} = -\sum_{\langle \mathbf{ij} \rangle} J\hat{\mathbf{S}}_\mathbf{i} \cdot \hat{\mathbf{S}}_\mathbf{j}$$

In a 1D chain, each of the spins has two neighbouring spins, for this reason, the Hamiltonian can be simplified to the following:

$$\hat{\mathcal{H}} = -2J\sum_{\mathbf{i}} \hat{\mathbf{S}}_\mathbf{i} \cdot \hat{\mathbf{S}}_{\mathbf{i+1}}$$

From this, the time dependence of $\langle \hat{\mathbf{S}}_\mathbf{j} \rangle$ can be calculated, leaving the following result:

$$\frac{d\langle \hat{\mathbf{S}}_\mathbf{j} \rangle}{dt} = \frac{1}{i\hbar}\langle [\hat{\mathbf{S}}_\mathbf{j}, \hat{\mathcal{H}}] \rangle$$

The spins at each site can now be treated as if they were classical vectors. If it is assumed that all spins are alligned along the z axis, the following normal mode solutions can then be obtained:

$$S_j^x = Ae^{(qja-\omega t)}$$

$$S_j^y = Be^{(qja-\omega t)}$$

and so $A = iB$, and therefore:

$$\hbar\omega = 4JS(1 - cos(qa))$$

Quantum Mechanical Approach

If we now address the quantum mechanical derivation, we must first look at the ground state of the system, $|\Phi\rangle$. $|\Phi\rangle$ takes into account all of the spins along the positive z direction meaning the 1D Hamiltonian for the Heisenberg model can be written like so:

$$\hat{\mathcal{H}} = -2J\sum_{\mathrm{i}}[\hat{\mathbf{S}}_{\mathbf{i}}^{\mathbf{z}}\hat{\mathbf{S}}_{\mathbf{i+1}}^{\mathbf{z}} + \frac{1}{2}(\hat{\mathbf{S}}_{\mathbf{i}}^{+}\hat{\mathbf{S}}_{\mathbf{i+1}}^{-} + \hat{\mathbf{S}}_{\mathbf{i}}^{-}\hat{\mathbf{S}}_{\mathbf{i+1}}^{+})]$$

Such that, $\hat{\mathcal{H}}|\Phi\rangle = NS^2J|\Phi\rangle$. If an excitation is to be induced, a spin at site j must be flipped. We must consider this state like so:

$$|j\rangle = \hat{S}_j^-|\Phi\rangle$$

This is the ground state of with the spin flipped at j. In doing so, the total spin of the system has been changed from 0 to 1. As a consequence of this the excitation now has an integer spin and can be treated as a boson. A Hamiltonian must now be applied to this new state, like so:

$$\hat{\mathcal{H}}|j\rangle = 2[(-NS^2J + 2SJ)|j\rangle - SJ|j+1\rangle - SJ|j-1\rangle]$$

We diagonalize the Hamiltonian in looking for plane wave solutions in the following form:

$$|q\rangle = \frac{1}{\sqrt{N}}\sum_{\mathrm{j}} e^{iqR_j}|j\rangle$$

$|q\rangle$ is a flipped spin that is smeared across all sites. As it is shown as states reperesting a single flipped spin, the total spin of $|q\rangle$ is $NS-1$, and so:

$$\hat{\mathcal{H}}|\Phi\rangle = E(q)|q\rangle$$

where

$$E(q) = -2NS^2J + 4JS(1 - cos(qa))$$

From this, it is clear that the energy of the excitation is given by:

$$\hbar\omega = 4JS(1 - cos(qa))$$

As with the semi-classical model.

References

Chapter 1

[1] G. Vidali, Superconductivity: the next revolution?, 5, 100, Cambridge [England], Cambridge University Press (1993).

[2] J. Waldram, Superconductivity of metals and cuprates, 2, Bristol [England], Institute of Physics Publishing (1996).

[3] L.N. Cooper, Phys. Rev. Lett **104**, 1189 (1956).

[4] J. G. Bednorz and K. A. Mueller, Z. Phys. B - Condensed Matter **64**, 189 (1986).

[5] J. Rossat-Mignod, L. P. Regnault, C. Vettier, P. Bourges, P. Burlet and J. Bossy, Physica C **185-189**, 86 (1991).

[6] P. G. Freeman, R. A. Mole, N. B. Christensen, A. Stunault and D. Prabhakaran, Physica B**536**, 720 (2018).

[7] J. Li, Y. Zhu, J. M. Tranquada, K. Yamada and D. J. Buttrey, Phys. Rev. B**67**, 012404 (2004).

[8] H. Yoshizawa, T. Kakeshita, R. Kajimoto, T. Tanabe, T. Katsufuji and Y. Tokura, Phys. Rev. B**61** 2, 854 (2000).

[9] P. G. Freeman, A. T. Boothroyd, D. Prabhakaran, M. Enderle and C. Niedermayer, Phys. Rev. B**70**, 024413 (2004).

[10] J. M. Tranquada, B. J. Sternlieb, J. D. Axe, Y. Nakamura and S. Uchida, Nature **375**, 561 (1995).

[11] M. Matsuda, M. Fujita, K. Yamada, R. J. Birgeneau, M. A. Kastner, H. Hiraka, Y. Endoh, S. Wakimoto and G. Shirane, Phys. Rev. B**62**, 9148 (2000).

[12] M. Fujika, K. Yamada, H. Hikara, P. M. Gehring, S. H. Lee, S. Wakimoto and G. Shirane, Phys. Rev. B**65**, 064505 (2002).

[13] C. H. Chen, S-W. Cheong and A. S. Cooper, Phys. Rev. Lett **71** 15, 2461 (1993).

[14] J. M. Tranquada, J. D. Axe, N. Ichikawa, Y. Nakamura, S. Uchida and B. Nachumi, Phys. Rev. B**54**, 7489 (1996).

[15] V. J. Emery, S. A. Kivelson and O. Zachar, Phys. Rev. B**56**, 6120 (1997).

[16] Yu. A. Krotov, D-H. Lee and A. V. Balatsky, Phys. Rev. B**56**, 8367 (1997).

[17] P. G. Freeman, D. Prabhakaran, K. Nakajima, A. Stunault, M. Enderle, C. Niedermayer, C. D. Frost, K. Yamada and A. T. Boothroyd, Phys. Rev. B**83** 9, 094414 (2011).

[18] M. Hüecker, M. V. Zimmermann, G. D. Gu, Z. J. Xu, J. S. Wen, Guangyong Xu, H. J. Kang, A. Zheludev and J. M. Tranquada, Phys. Rev. B**83**, 104506 (2011).

[19] A. T. Boothroyd, P. G. Freeman, D. Prabhakaran, A. Hiess, M. Enderle, J. Kulda, and F. Altorfer, Phys. Rev. Lett. **91**, 257201 (2003).

[20] K. Ishizaka, T. Arima, Y.Murakami, R. Kajimoto, H. Yoshizawa, N. Nagaosa and Y. Tokura, Phys. Rev. Lett**92** 19, 196404 (2004).

[21] P. Wochner, J. M. Tranquada, D. J. Buttery and V. Sachan, Phys. Rev B**57** 2, 1066 (1998).

[22] P. G. Freeman, A. T. Boothroyd, D. Prabhakaran, M. Enderle and C. Niedermayer, Phys. Rev. B **70**, 024413 (2004).

[23] Ill.eu. (2018). [online] Available at: https://www.ill.eu/users/instruments/instruments-list/in12/description/instrument-layout/ [Accessed 7 Nov. 2018].

[24] Tf.uni-kiel.de. (2019). Float Zone Crystal Growth. [online] Available at: https://www.tf.uni-kiel.de/matwis/amat/elmaten/kap6/advanced/t613.html [Acc-

essed 7 Jan. 2019].

[25] D. Prabhakaran, P. Isla and A. T. Boothroyd, J. Cryst. Growth **237**, 815 (2002).

[26] G. Shirane, S. M. Shapiro and J. M. Tranquada (2006). Neutron scattering with a triple axis spectrometer. Cambridge: Cambridge Univ Press.

[27] G. Squires, (2012). Introduction to the theory of thermal neutron scattering. Cambridge: Cambridge University Press.

[28] K. Schmalzl, W. Schmidt, S. Raymond, H. Feilbach, C. Mournier, B. Vettard and T. Brückel, Nucl. Instrum. Meth. A, **819** (2016).

[29] E. Kisi and J. Howard, Applications of Neutron Powder Diffraction, Oxford Series on Neutron Scattering in Condensed Matter, Volume 15. Oxford Scholarship Online. 52 (2008).

[30] G. Bacon, Neutron diffraction, 5, Oxford [England], Oxford University Press (1975).

[31] W. Schmidt and B. Fák, New focusing analyser on IN12 (ILL-RA–1998). Leadbetter, Alan J. (Ed.). [France] (1999).

[32] W. Schmidt and M. C. Rheinstädter, S. Raymond, M. Ohl, Physica B**350**, e849 (2004).

Chapter 2

[1] G. Shirane, S. M. Shapiro and J. M. Tranquada (2006). Neutron scattering with a triple axis spectrometer. Cambridge: Cambridge Univ Press.

[2] S. Blundell, (2014). Magnetism in condensed matter. Oxford: Oxford University Press.

[3] G. Squires, (2012). Introduction to the theory of thermal neutron scattering. Cambridge: Cambridge University Press.

[4] Ill.eu. (2019). [online] Available at: https://www.ill.eu/about-the-ill/what-is-the-ill/ill-faq/ [Accessed 5 Jul. 2019].

[5] P. G Freeman, (2005). Magnetism and Magnetic Excitations of Charge Ordered $La_2 - xSr_xNiO_4 + \delta$. PhD. University of Oxford.

[6] Ill.eu. (2019). [online] Available at: https://www.ill.eu/reactor-and-safety/high-flux-reactor/technical-characteristics/ [Accessed 5 Jul. 2019].

[7] J. Goldstone, A. Salam and S. Weinberg, Phys. Rev **127** 3, 965 (1962).

[8] C. Kittel (2005). Introduction to solid state physics. New York: Wiley.

[9] H. Woo, A. T. Boothroyd, K. Nakajima, T. G. Perring, C. D. Frost, P. G Freeman, D. Prabhakaran, K. Yamada and J. M. Tranquada, Phys. Rev B**72** 6, 064437 (2005).

Chapter 3

[1] P. G. Freeman, A. T. Boothroyd, D. Prabhakaran, M. Enderle and C. Niedermayer, Phys. Rev. B**70** 2, 024413 (2004).

[2] K. Ishizaka, T. Arima, Y. Murakami, R. Kajimoto, H. Yoshizawa, N. Nagaosa and Y. Tokura, Phys. Rev. Lett. **92** 19, 196404 (2004).

[3] P. G. Freeman, N. B. Christensen, D. Prabhakaran and A. T. Boothroyd, J. Phys.: Conf. Ser. **200** 0123037 (2010).

[4] S-H. Lee, Y-C Lai, C-H. Du, A. F. Siegenfeld, Y-J. Kao, P. D. Hatton, D. Prabhakaran, Y. Su and D-J. Huang, Phys. Rev. B**92**, 205114 (2015).

[5] A. T. Boothroyd, P. G. Freeman, D. Prabhakaran, A. Hiess, M. Enderle, J. Kulda and F. Altorfer, Phys. Rev. Lett. **91**, 257201 (2003).

[6] S. R. Giblin, P. G Freeman, K. Hradil, D. Prabhakaran and A. T. Boothroyd, Phys. Rev. B**78**, 184423 (2008).

[7] P. G. Freeman, Personal Communication, (2019).

[8] S. Blundell, (2014). Magnetism in condensed matter. Oxford: Oxford University Press.

[9] Squid.iitd.ernet.in. (2019). SQUID National Facility, IIT Delhi. [online] Available at: http://squid.iitd.ernet.in/BasicLiterature.htm [Accessed 14 Nov. 2019].

[10] P. D. Hatton, M. E. Ghazi, S. B. Wilkins, P. D. Spencer, D. Man-nix, T. dÁlmeida, D. Prabhakaran, A. T. Boothroyd and S-W. Cheong, Physica B**318**, 289 (2002).

Chapter 4

[1] P. G. Freeman, D. Prabhakaran, K. Nakajima, A. Stunault, M. Enderle, C. Niedermayer, C. Frost, K. Yamada and A. T. Boothroyd, Phys. Rev. B, **83** 9 (2011).

[2] J. Goldstone, A. Salam and S. Weinberg, Phys. Rev **127** 3, 965 (1962).

[3] P. G. Freeman, A. T. Boothroyd, R. A. Ewings, M. Hücker, D. Prabhakaran, M. Enderle and J. M. Tranquada, J. Phys.: Condens. Matter **20**, 104229 (2008).

[4] Nuclear Power. (2019). Neutron Energy. [online] Available at: https://www.nuclear-power.net/nuclear-power/reactor-physics/atomic-nuclear-physics/fundamental-particles/neutron/neutron-energy/ [Accessed 2 Sep. 2019].

Chapter 5

[1] K. Ishizaka, T. Arima, Y. Murakami, R. Kajimoto, H. Yoshizawa, N. Nagaosa and Y. Tokura, Phys. Rev. Lett. **92** 19, 196404 (2004).

[2] S-H. Lee, Y-C Lai, C-H. Du, A. F. Siegenfeld, Y-J. Kao, P. D. Hatton, D. Prabhakaran, Y. Su, and D-J. Huang, Phys. Rev. B**92**, 205114 (2015).

[3] P. G. Freeman, N. B. Christensen, D. Prabhakaran and A. T. Boothroyd, J. Phys.: Conf. Ser. **200**, 0123037 (2010).

[4] P. G. Freeman, A. T. Boothroyd, R. A. Ewings, M. Hücker, D. Prabhakaran, M. Enderle and J. M. Tranquada, J. Phys.: Condens. Matter **20**, 104229 (2008).

[5] S. R. Giblin, P. G Freeman, K. Hradil, D. Prabhakaran and A. T. Boothroyd, Phys. Rev. B**78**, 184423 (2008).

[6] J. Goldstone, A. Salam and S. Weinberg, Phys. Rev **127** 3, 965 (1962).